universität
wien

MASTERARBEIT | MASTER'S THESIS

Titel | Title

Experimental Realization of Inverse-Design Magnonics

verfasst von | submitted by

Fabian Majcen BSc

angestrebter akademischer Grad | in partial fulfilment of the requirements for the degree of

Master of Science (MSc)

Wien | Vienna, 2024

Studienkennzahl lt. Studienblatt | Degree programme code as it appears on the student record sheet:	UA 066 876
Studienrichtung lt. Studienblatt | Degree programme as it appears on the student record sheet:	Masterstudium Physics
Betreut von | Supervisor:	Univ.-Prof. Dr. habil. Andrii Chumak

Acknowledgements

I would like to express my deepest gratitude to Prof. Andrii Chumak, who inspired me early in my bachelor's studies during the seminar "Research at the Faculty of Physics" in 2019. His presentation of his research was both approachable and engaging, sparking my interest in the fascinating world of spin waves. When it was time to choose a topic for my bachelor's thesis, I contacted Prof. Chumak, and under the additional supervision of Noura Zenbaa, we found a suitable topic. Noura Zenbaa played a crucial role in teaching me how to work in the lab, providing guidance and support throughout my project.

After completing my degree, they invited me to join their team to work on this exciting project. I am incredibly grateful for the trust they placed in me and for the opportunity to be part of their group. Over the past two years, we have worked persistently, and I am proud to present the results of our efforts. I am thankful for all the skills I have acquired along the way, including training in presentations and scientific writing. Their mentorship has been invaluable, and I am grateful for their continued support and encouragement.

I would also like to express my gratitude to Dr. Claas Abert for his assistance and guidance in developing the device drivers in Python, as well as his support with the magnum.pi software for micromagnetic simulations.

Furthermore, I would like to thank the Vienna Doctoral School in Physics (VDSP), particularly its Scientific Director, Prof. Markus Arndt, for granting me a Master Fellowship. This opportunity allowed me to extend my work by six additional months.

Next, I want to thank my colleagues and friends Sebastian Knauer, Khrystyna Levchenko, Barbora Budinská, Sebastian Lamb-Camarena, Kristýna Davídková, Andrey Voronov, Rostyslav Serha, David Schmoll, Clemens Schmid, Andreas Höfinger, Simon Peinhaupt and Pedro del Real Lavergne for the engaging discussions and for creating such a positive and enjoyable work environment.

Lastly, I would also like to thank my family and friends for their constant encouragement and support. I am especially thankful to my girlfriend, Lisa, for her unending support and belief in me through this entire journey.

Abstract

The field of magnonics, which utilizes magnons—the quanta of spin waves—for energy-efficient data processing, has seen advancements through developments in inverse design. Inverse design involves specifying a desired functionality and using computational algorithms to determine the device design that achieves it.

This study represents a pioneering experimental demonstration of an inverse-design magnonic processor capable of implementing radio frequency functionalities. Building on previous work in inverse design magnonics, which has primarily relied on complex numerical simulations, this device introduces a novel approach by enabling reconfiguration on a nanosecond timescale and direct experimental evaluation of states. The device features a square array of 49 independent direct current loops, which generate a complex magnetic landscape. Due to this intricate setup, spin waves propagating through a rectangular yttrium iron garnet film undergo multiple scatterings, resulting in significant changes in direction, wavelength, and phase due to both linear and nonlinear effects. These phenomena are harnessed to implement various RF functionalities.

The capabilities of the device are demonstrated through its application as an RF notch filter, successfully realized across a broad spin-wave frequency spectrum, and a frequency demultiplexer. Additional investigations into spin-wave nonlinearity provide deeper insights into its impact on performance. A direct search optimization and a genetic algorithm are used to configure the field patterns, showcasing the device's versatility and effectiveness in achieving tailored functionalities. These results highlight the potential of inverse-design magnonic devices for advanced RF applications and open up new possibilities for dynamic, reconfigurable magnonic systems.

Kurzfassung

Das Feld der Magnonik, das Magnonen—die Quanten der Spinwellen—für energieeffiziente Datenverarbeitung nutzt, hat durch Entwicklungen im Bereich des inversen Designs bedeutende Fortschritte gemacht. Inverses Design umfasst die Festlegung einer gewünschten Funktionalität und die Nutzung von Rechenalgorithmen zur Bestimmung des Geräteentwurfs.

Diese Studie stellt eine wegweisende experimentelle Demonstration eines invers-gestalteten magnonischen Prozessors dar, der in der Lage ist, Radiofrequenzfunktionalitäten zu implementieren. Aufbauend auf bisheriger Forschung im Bereich des inversen Designs in der Magnonik, die überwiegend auf komplexen numerischen Simulationen basieren, führt dieses Gerät einen neuartigen Ansatz ein, indem es eine Neukonfiguration im Nanosekundenbereich und die direkte experimentelle Evaluierung von Zuständen ermöglicht. Das Gerät besteht aus einer quadratischen Matrix von 49 unabhängigen Gleichstrom-Schleifen, die eine komplexe magnetische Landschaft erzeugen. Aufgrund dieses komplexen Aufbaus durchlaufen Spinwellen, die sich durch einen rechteckigen Yttrium-Eisen-Granat-Film ausbreiten, mehrfache Streuungen, was zu signifikanten Änderungen in Richtung, Wellenlänge und Phase aufgrund sowohl linearer als auch nichtlinearer Effekte führt. Diese Phänomene werden genutzt, um verschiedene RF-Funktionalitäten zu implementieren.

Die Fähigkeiten des Geräts werden durch seine Anwendung als RF-Kerbfilter, der erfolgreich über ein breites Spektrum von Spinwellenfrequenzen realisiert wurde, und als Frequenz-Demultiplexer demonstriert. Zusätzliche Untersuchungen zur Spinwellen-Nichtlinearität bieten tiefere Einblicke in deren Auswirkungen auf das Leistungsvermögen. Eine Direct Search Optimierung und ein genetischer Algorithmus, werden verwendet, um die Feldmuster zu konfigurieren, was die Vielseitigkeit und Effektivität des Geräts bei der Umsetzung maßgeschneiderter Funktionalitäten demonstriert. Diese Ergebnisse unterstreichen das Potenzial von invers-gestalteten magnonischen Geräten für fortgeschrittene RF-Anwendungen und eröffnen neue Möglichkeiten für dynamische, rekonfigurierbare magnonische Systeme.

Contents

List of Figures

List of Abbreviations

AC	Alternating Current
BVMSW	Backward Volume Magnetostatic Spin Waves
CPW	Coplanar Waveguide
DC	Direct Current
DS	Direct Search
FIB	Focused-Ion-Beam
FMR	Ferromagnetic Resonance
FVMSW	Forward Volume Magnetostatic Spin Waves
FWHM	Full Width at Half Maximum
GA	Genetic Algorithm
GGG	Gadolinium Gallium Garnet
IoT	Internet of Things
LLG	Landau–Lifshitz–Gilbert
LPE	Liquid-Phase Epitaxy
MSW	Magnetostatic Spin Waves
MSSW	Magnetostatic Surface Spin Waves
PCB	Printed Circuit Board
PMA	Perpendicular Magnetic Anisotropy
PSWS	Propagating Spin-Wave Spectroscopy
PSSW	Perpendicular Standing Spin Wave
RF	Radio Frequency
SCPI	Standard Commands for Programmable Instruments
TEM	Transverse Electromagnetic Mode
trMOKE	Time-Resolved Magneto-Optical Kerr Effect
VISA	Virtual Instrument Software Architecture
YIG	Yttrium Iron Garnet

1 Introduction

Spin waves are collective excitations of spins in magnetically ordered materials. In the field of magnonics, named after magnons—the quanta of spin waves—research focuses on the transmission, storage, and processing of information using spin waves [1]. Utilizing magnons as data carriers, instead of electrons as in traditional electronics, could bring numerous advantages. Since magnon currents do not involve the motion of particles, Joule heating is eliminated. Additionally, wave-based computing introduces an extra degree of freedom, enabling operations with vector variables. The pronounced nonlinear phenomena of spin waves also allow for the manipulation of one signal by another. Moreover, even nanosized structural elements are feasible, as spin wave wavelengths are only limited by the lattice constant of the magnetic materials [2].

Magnonics holds significant potential for radio frequency (RF) applications, especially within the rapidly evolving domains of the Internet of Things (IoT), 5G, and future 6G technologies. Over the past three decades, mobile communication has experienced an unprecedented surge in users, data transmission volumes, and efforts in research and development [3]. These frameworks demand RF devices capable of high-speed and high-capacity wireless communication, crucial for mobile phones, autonomous vehicles, smart cities, and advanced healthcare monitoring systems [4]. This drives the necessity for RF components that are versatile, energy-efficient, and capable of flexible operation across different frequencies and bandwidths.

Spin waves, with their ability to propagate without particle movement, offer an energy-efficient solution for data transfer and processing within a wide frequency range from 1 GHz to hundreds of THz, covering the spectrum of both 5G and 6G technologies [2, 5]. Furthermore, the nonlinear and nonreciprocal properties of spin waves present unique opportunities for developing RF devices [6, 7].

New perspectives for information processing have been opened up by utilizing the concept of inverse design. This involves defining a functionality by a human and then a computational algorithm searches for the device design that satisfies the requested functionality. In the field of photonics inverse design is already employed for many functionalities. Using photons as data carriers, inverse-designed demultiplexers [8], synapes [9], and neurons [10] have been developed. Specialized processors capable of solving inverse problems experimentally have been demonstrated. Complex reconfigurable photonic media, such as spatial light modulators or heater arrays, enabled the realization of vowel recognition, multimode interference power splitters, and a photonic emulator for single and multimode photonic devices [11, 12, 13].

Adopting inverse design in magnonics has sparked a wave of innovative research [14]. Magnonic (de)multiplexers, nonlinear switches, Y-circulators [15], lenses [16], and neuromorphic networks for vowel recognition [17] have been demonstrated. However, these approaches depend on complex numerical computational algorithms that are both time- and energy-consuming. Once a solution is obtained through the inverse process, devices must be fabricated and tested with fixed functionalities. This thesis employs a reconfigurable magnonic medium, allowing the inverse problem to be solved directly in the experiment. This enables switching between functionalities and reduces the time required per iteration compared to simulation-based methods.

The reconfigurable magnonic device employs a 7×7 matrix of direct current loops, which can generate a static magnetic field with 2048 discrete steps, providing approximately 10^{162} degrees of freedom. Spin waves traveling through this intricate magnetic field landscape experience multiple scatterings, resulting in changes to their direction, wavelength, and phase due to both linear and nonlinear effects. The device's field patterns are configured using advanced algorithms, such as Direct Search optimization and Genetic Algorithm, to achieve specific functionalities. In this thesis, the device is demonstrated with a RF notch filter and a demultiplexer, showcasing its capabilities. The design, however, possesses the potential to realize a wide range of other functionalities, underscoring its versatility and adaptability.

Following this introduction chapter, Chapter 2 provides the necessary theoretical background. The motion of a magnetic moment in a magnetic field is described (Landau–Lifshitz–Gilbert equation) and built on to understand spin wave propagation with additional insight on their propagation dynamics and interactions. Chapter 3 reviews the state of the art in inverse-design magnonics by analyzing pioneering works in the field. Then, in Chapter 4, the experimental setup, spin wave excitation with microstrip antennas, the reconfigurable magnonic medium and the remote control of the devices is discussed. In Chapter 5 the experimental results are presented and discussed in Chapter 6. Finally, Chapter 7, provides a general summary and outlook on future developments in this emerging field of research.

2 Theoretical Background

2.1 Maxwell's Equations

The Maxwell equations are a set of fundamental laws that form the foundation for understanding classical electromagnetism, optics, and electric circuits. Formulated by James Clerk Maxwell in the 19th century, these equations describe the interaction of electric and magnetic fields and their propagation through space and time. The Maxwell equations are as follows:

$$\operatorname{div}\vec{E} = \frac{\rho}{\epsilon_0}, \tag{2.1}$$

$$\operatorname{div}\vec{B} = 0, \tag{2.2}$$

$$\operatorname{rot}\vec{E} = -\frac{\partial\vec{B}}{\partial t}, \tag{2.3}$$

$$\operatorname{rot}\vec{B} = \mu_0\vec{j} + \frac{1}{c^2}\frac{\partial\vec{E}}{\partial t}. \tag{2.4}$$

With the electric field $\vec{E}$, the magnetic field $\vec{B}$, the displacement current $\vec{j}$, the electric charge density ρ, the permittivity of free space ϵ_0, the permeability of free space μ_0, and the speed of light c [18]. Figure 2.1 illustrates the Maxwell equations. Figure 2.1a shows how electric charges act as sources of electric fields (Equation 2.1). In contrast, Equation 2.2 establishes that magnetic monopoles do not exist. Figure 2.1b depicts how a time-varying magnetic field induces a rotational electric field (Equation 2.3). Figure 2.1c depicts the first part of Equation 2.4 which relates the magnetic field to the electric current. This rotational magnetic field generated by electric currents is also called “Oersted field”. The second part of Equation 2.4, shown in Figure 2.1d, illustrates how a time-varying electric field induces a rotational magnetic field, similar to Equation 2.3 but with an inverted sign.

2.1.1 Biot–Savart law

The Biot–Savart law describes the magnetic field created by a constant electric current I. A current-carrying conductor with the infinitesimal length element $d\vec{l}$ at $\vec{r'}$ creates the magnetic induction

$$d\vec{B}(\vec{r}) = \frac{\mu_0}{4\pi} I d\vec{l} \times \frac{\vec{r} - \vec{r'}}{|\vec{r} - \vec{r'}|^3} \tag{2.5}$$

at the point $\vec{r}$. It is a specialized case of Maxwell's fourth equation (Equation 2.4) [19].

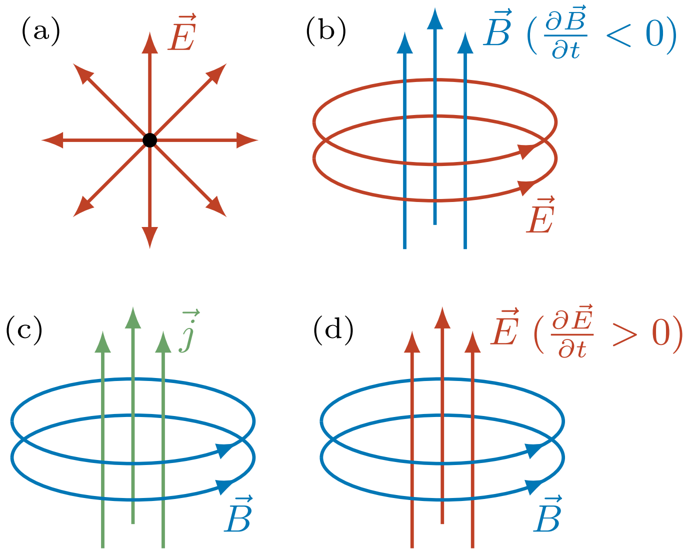

Figure 2.1: Illustration of Maxwell's equations. (a) Electric charges act as a source of electric fields (Equation 2.1). (b) A time-varying magnetic field induces a rotational electric field (Equation 2.3). (c) Electric currents generate an Oersted field (first part of Equation 2.4). (d) A time-varying electric field induces a rotational magnetic field (second part of Equation 2.4).

2.2 Landau–Lifshitz–Gilbert Equation (LLG)

The Landau–Lifshitz–Gilbert equation (LLG) describes the time evolution of a magnetic moment $\vec{m}$ (or a magnetization $\vec{M}$) in an effective magnetic field $\vec{H}_{\text{eff}}$:

$$\frac{\partial \vec{m}}{\partial t} = -\gamma \vec{m} \times \vec{H}_{\text{eff}} + \alpha \vec{m} \times \frac{\partial \vec{m}}{\partial t} \tag{2.6}$$

With the reduced gyromagnetic ratio $\gamma = \mu_0 \gamma_e \approx 2.2128 \cdot 10^5\,\mathrm{m\,A^{-1}\,s^{-1}}$ and the Gilbert damping parameter α. When the magnetic moment and the magnetic field are not aligned, the magnetic moment undergoes precessional motion around the magnetic field axis. This behavior is described by the first term of the equation ($\propto \vec{m} \times \vec{H}_{\text{eff}}$) and is illustrated in Figure 2.2a. The second term of the equation ($\propto \vec{m} \times \frac{\partial \vec{m}}{\partial t}$) describes the damping of the precession, which is depicted in Figure 2.2b. This damping effect leads to the magnetic moment eventually aligning with the magnetic field. The magnetic moment in this context refers to those within a magnetic material, and the energy lost due to damping is primarily transferred to lattice vibrations. Consequently, the magnetic moment spirals until it aligns with the magnetic field, as shown in Figure 2.2c [20, 21].

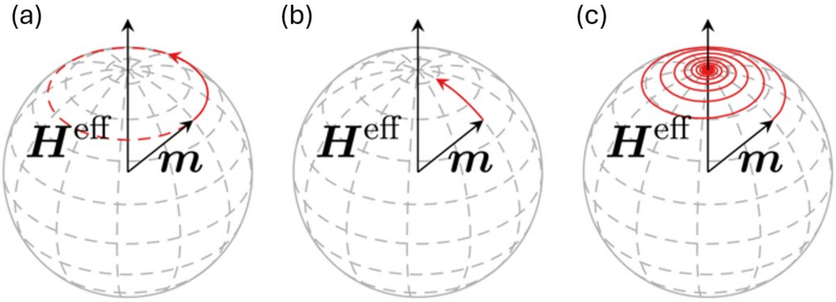

Figure 2.2: Visualization of a magnetic moment $\vec{m}$ interacting with a magnetic field $\vec{H}_{\text{eff}}$. Panel (a) displays precessional motion, (b) shows damping effects, and (c) demonstrates the resultant spiral trajectory (taken from [21]).

2.3 Magnetostatic Spin Waves (MSW)

Spin waves are excitations that occur in magnetic materials where magnetic order exists between neighboring spins, such as in ferro-, antiferro-, or ferrimagnetic materials. When spins are disturbed and no longer aligned with the magnetization, they begin to precess as described in Section 2.2 (Equation 2.6 and Figure 2.2). Through dipole-dipole and exchange interactions, a precessing spin excites neighboring spins, resulting in a collective precession that propagates through the material, forming what is known as a spin wave. The quantized quasiparticle associated with spin waves is called a magnon [20].

In magnetostatic spin waves (MSW), the primary interaction between spins is the dipole-dipole interaction, which is why they are often referred to as dipolar spin waves. The name “magnetostatic” indicates that the solutions to Maxwell’s equations are derived under a magnetostatic approximation, which assumes that the spin-wave wavelengths are much shorter than those of electromagnetic waves of the same frequency, and that the displacement current is negligible. The exchange interaction, which is highly sensitive to the relative orientation of neighboring spins, is also neglected in this context because it is significant only for shorter wavelengths. Since MSWs have much larger wavelengths, ranging from micrometers to millimeters, the influence of the exchange interaction is negligible [1]. In the limit of an infinite wavelength ($\lambda \to \infty$ or equivalently $k \to 0$), the precessing spins are all in phase with each other. This phenomenon is known as ferromagnetic resonance (FMR). The frequency at which this resonance occurs is called the ferromagnetic resonance frequency f_{FMR}, which depends on the shape of the sample [22, 23].

Magnetostatic spin waves are categorized into three distinct modes: magnetostatic surface spin waves (MSSW), forward volume magnetostatic spin waves (FVMSW), and backward volume magnetostatic spin waves (BVMSW). Each mode exhibits unique dispersion characteristics. The key difference between these modes lies in the relative orientation of the propagation direction with respect to the applied bias magnetic field, which is used to magnetize the sample [1]. Figure 2.3 illustrates these orientations for

MSSW (a), FVMSW (b) and BVMSW (c).

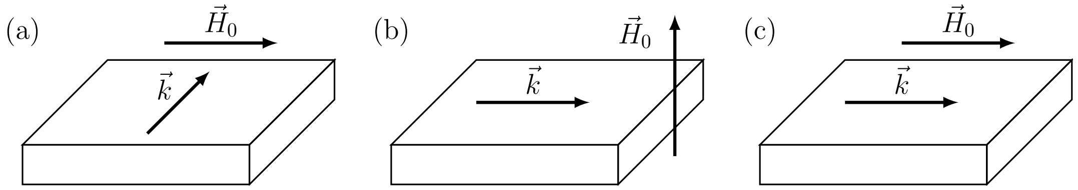

Figure 2.3: Three magnetostatic spin wave modes emerge from different relative orientations between the propagation direction $\vec{k}$ and the applied bias magnetic field $\vec{H}_0$: (a) Magnetostatic surface spin waves (MSSW), (b) forward volume magnetostatic spin waves (FVMSW) and (c) backward volume magnetostatic spin waves (BVMSW).

2.3.1 Dispersion Relation

The dispersion relation describes the relationship between the wavenumber k and the frequency f of a wave. Based on the previously discussed magnetostatic approximation, the dispersion relations for the three magnetostatic spin wave modes in an infinite slab can be derived:

- MSSW:

$$f_{\mathrm{MSSW}}(k) = \sqrt{\left(f_{\mathrm{H}} + \frac{f_{\mathrm{M}}}{2}\right)^2 - \left(\frac{f_{\mathrm{M}}}{2}\right)^2 \mathrm{e}^{-2kd}} \tag{2.7}$$

- FVMSW:

$$f_{\mathrm{FVMSW}}(k) = \sqrt{f_{\mathrm{H}}\left(f_{\mathrm{H}} + f_{\mathrm{M}}\left(1 - \frac{1-\mathrm{e}^{-kd}}{kd}\right)\right)} \tag{2.8}$$

- BVMSW:

$$f_{\mathrm{BVMSW}}(k) = \sqrt{f_{\mathrm{H}}\left(f_{\mathrm{H}} + f_{\mathrm{M}}\frac{1-\mathrm{e}^{-kd}}{kd}\right)} \tag{2.9}$$

$$f_{\mathrm{H}} = \frac{\gamma\mu_0 H_0}{2\pi}, \quad f_{\mathrm{M}} = \frac{\gamma\mu_0 M_{\mathrm{eff}}}{2\pi}$$

With the sample thickness d, the applied magnetic field H_0 , the effective saturation magnetization M_{eff}, the magnetic permeability of free space μ_0 and the gyromagnetic ratio $\gamma = 1.76 \cdot 10^{11}\,\mathrm{rad\,s^{-1}\,T^{-1}}$ [1]. The effective saturation magnetization

$$M_{\mathrm{eff}} = M_{\mathrm{S}} - H_{\mathrm{a}} - H_{\mathrm{demag}} \tag{2.10}$$

depends on the saturation magnetization M_{S}, the magnetocrystalline anisotropy field H_{a} and the demagnetizing field H_{demag}.

The magnetocrystalline anisotropy field is an intrinsic property of the material that depends on its crystal geometry and tends to align the magnetization along specific crystal axes of symmetry [22]. For electron orbitals that are not spherically symmetric, the energy of the state varies with its orientation relative to the surrounding ions in the crystal. Due to spin-orbit coupling, the energy of the net moment depends on its alignment with respect to the major axes of the crystal. In yttrium iron garnet (further discussed in Section 2.5) the iron ions in the ground state have no orbital angular momentum and therefore no spin–orbit coupling or magnetocrystalline anisotropy should occur. Nonetheless, experimentally a small anisotropy energy contribution can be found. The reason for this is likely due to small spin–orbit interactions among the electronic sub-states neglected in the coupling scheme [20].

The demagnetizing field is a magnetic field generated by a sample or material as it becomes magnetized. This field can be interpreted as arising from free magnetic poles distributed on the surface of the material. These surface poles create an internal field that opposes the magnetization of the material. The magnitude of the demagnetizing field is highly dependent on the shape and size of the sample. This phenomenon explains why magnetic bodies, such as bar magnets, tend to favor magnetization along their longer axes [24]. For magnetostatic surface spin waves or backward volume magnetostatic spin waves, the demagnetizing field can often be neglected due to the in-plane magnetization and the assumption of a thin film. However, for forward volume magnetostatic spin waves, the demagnetizing field plays a significant role.

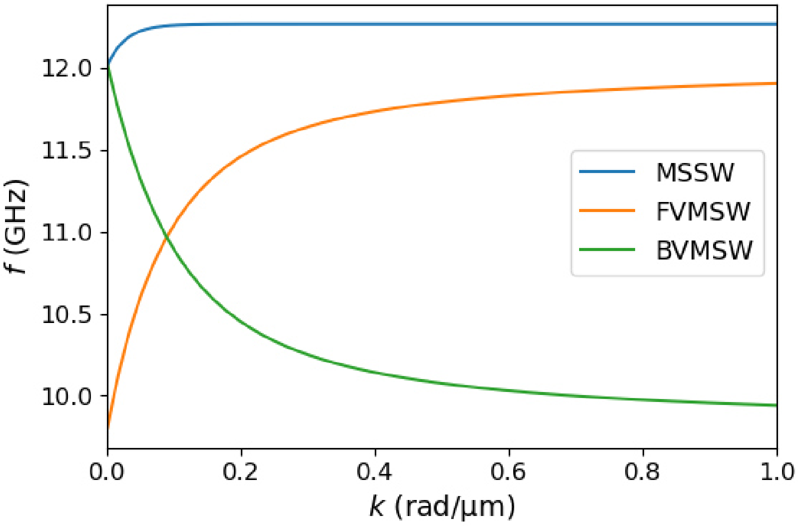

Figure 2.4: Dispersion relation of the three magnetostatic spin wave modes for a sample of thickness $d = 18\,\mu\mathrm{m}$ at a magnetic field of $B = 350\,\mathrm{mT}$ with a saturation magnetization of $M_{\mathrm{eff}} = M_{\mathrm{S}} = 140\,\mathrm{kA\,m^{-1}}$.

Figure 2.4 shows the dispersion relation of the magnetostatic spin wave modes for a sample of thickness $d = 18\,\mu\mathrm{m}$ at a magnetic field of $B = 350\,\mathrm{mT}$ with a saturation magnetization of $M_{\mathrm{eff}} = M_{\mathrm{S}} = 140\,\mathrm{kA\,m^{-1}}$.

2.3.2 Forward Volume Magnetostatic Spin Waves (FVMSW)

For FVMSW, the magnetization is out of plane with spin waves propagating perpendicular to the magnetic field (Figure 2.2b). The dispersion depicted in Figure 2.4 illustrates only the lowest order mode of FVMSW ($\mathrm{n} = 0$), characterized by a constant spin wave amplitude throughout the thickness of the magnetic material. However, higher-order thickness modes also exist, exhibiting a sinusoidally distributed spin wave amplitude. This amplitude distribution through the volume of the thickness is shown in Figure 2.5 for the first few thickness modes. The thickness mode number n also relates to the number of zero amplitude points. All of these modes have the same cutoff frequency, therefore, there is no frequency range where only a single mode propagates [20, 25].

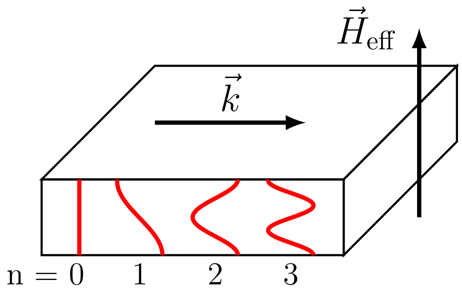

Figure 2.5: Thickness modes of FVMSW showing sinusoidal distributed spin wave amplitude through the volume of the magnetic material.

In contrast to the other two types of magnetostatic spin waves, the dispersion of FVMSW does not change with the in-plane propagation direction of the spin wave. The orientation between the wavevector and the bias field remains orthogonal, resulting in isotropic propagation of FVMSW in the plane of the film. However, this holds true only under the assumption of an isotropic material. Considering magnetocrystalline anisotropy will give rise to anisotropic propagation characteristics. The phase and group velocities of FVMSW have the same direction and only differ in magnitude. Waves with this property are called “forward waves”. This characteristic, the propagation through the whole volume of the material, and the use of the magnetostatic approximation give them the name “forward volume magnetostatic spin waves” [20].

A very important and practical property of the spin wave dispersion is the influence of the bias magnetic field. By simply increasing or decreasing the magnetic field, the dispersion shifts up or down, allowing the propagation frequency range of the spin wave to be modified as needed. This characteristic is illustrated in Figure 2.6 by plotting the dispersion of FVMSW (Equation 2.8) for various magnetic field strengths. Additionally, the figure can be viewed as an example of the influence of the demagnetizing field in the FVMSW configuration. Given that the demagnetizing field reduces the internal magnetic field within the sample, this reduction leads to a shift in the spin wave spectrum to lower

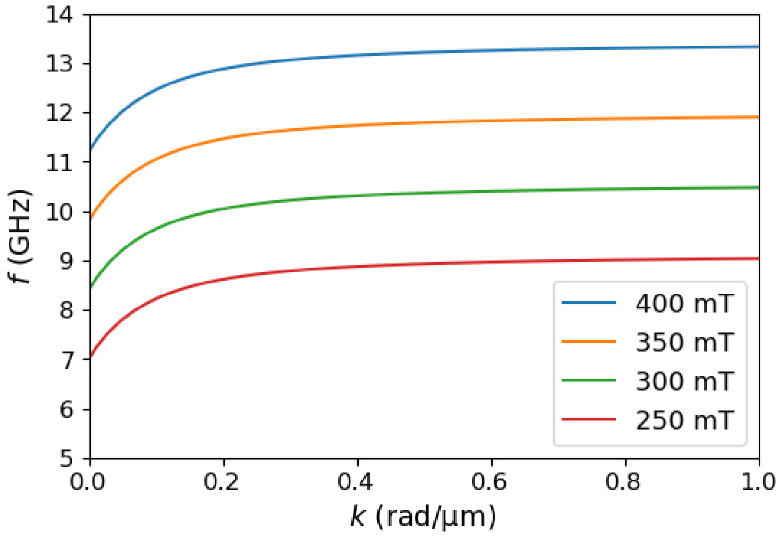

Figure 2.6: Dispersion relation of FVMSW for magnetic field strengths B of 250 mT, 300 mT, 350 mT and 400 mT ($d = 18\,\mu\mathrm{m}$, $M_{\mathrm{eff}} = M_{\mathrm{S}} = 140\,\mathrm{kA\,m^{-1}}$).

frequencies compared to the other MSW modes (Figure 2.4).

2.4 Nonlinear Spin Wave Interactions

Nonlinearity is fundamental for data processing, allowing one signal to manipulate another. This principle is the basis of all modern electronics, as it is the mechanism used in semiconductor transistors. Spin waves exhibit a variety of pronounced nonlinear phenomena, making them promising for radio frequency applications, Boolean computing, and neuromorphic computing [2, 26].

2.4.1 Large-Amplitude Spin Waves

The impact of the demagnetizing field was already discussed in Section 2.3.1. For a out-of-plane magnetized film (FVMSW) this effect significantly reduces the magnetic field inside the sample. The lowest order nonlinear effect arises from large-amplitude spin waves. As the cone angle of precession θ increases the z-component of the magnetization is reduced by the factor $\cos\theta$. Consequently, the demagnetizing field decreases which results in an increase in frequency of the uniform precessing band edge by

$$\Delta f = f_{\mathrm{M}}(1 - \cos\theta) \approx f_{\mathrm{M}}\frac{\theta^2}{2}. \tag{2.11}$$

Spin waves at $k = 0$ with nearly circular magnetization precession around the film normal are assumed. Relating the precession angle to the power P in the uniform precession spin wave, the shift in the lower edge of the passband can be estimated as

$$\frac{\Delta f}{P} = \frac{f_\mathrm{M}}{f} \frac{2}{M_\mathrm{S}^2 d^2 \mu_0 \pi}. \tag{2.12}$$

Equation 2.12 predicts a linear shift towards higher frequencies as the cone angle of the precession increases [20].

2.4.2 Magnon–Magnon Interactions

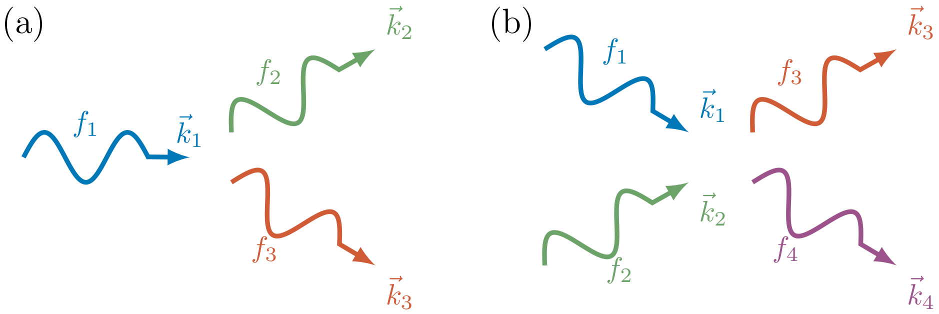

Figure 2.7: Magnon-magnon interaction: (a) Three magnon splitting, (b) Four-magnon scattering. With frequencies f_i and wave vectors $\vec{k}_i$.

Figure 2.7 shows the most common magnon-magnon interactions: The three magnon splitting and the four-magnon scattering. A variety of other scattering processes with a larger number of participating magnons are possible as well; however, the probability of these processes occurring decreases with the increasing number of participating quasiparticles [25].

Three-Magnon Splitting

In the three-magnon splitting process, one magnon is annihilated while two magnons are created. Similarly, in the three-magnon confluence process, two magnons combine to form a single magnon. Considering momentum and energy conservation for the three-magnon splitting leads to the conditions

$$f_1 = f_2 + f_3 \tag{2.13}$$

and

$$\vec{k}_1 = \vec{k}_2 + \vec{k}_3. \tag{2.14}$$

However, since the number of magnons is not conserved, angular momentum is also not conserved. The interaction involves the transfer of magnon spin to the lattice and is primarily driven by dipole-dipole interactions. Additionally, these processes are constrained by the spin wave dispersion; the scattered spin wave must fall within the spin wave spectrum of the system [25, 20].

Four-Magnon Scattering

Four-magnon scattering involves the interaction of two magnons, resulting in the creation of two different magnons. The conservation laws state

$$f_1 + f_2 = f_3 + f_4 \tag{2.15}$$

and

$$\vec{k}_1 + \vec{k}_2 = \vec{k}_3 + \vec{k}_4. \tag{2.16}$$

In this case, scattering can occur across the entire spin wave spectrum [25, 20]. The four-magnon scattering process is highly dependent on the spin wave excitation power. Higher power results in increased scattering of spin waves to different frequencies, which in turn causes the intensity of the excited spin waves to saturate. While a comprehensive theoretical description of this scattering process has been developed for continuous thin films, spin wave dynamics in small magnetic structures exhibit different behavior. The confinement in these structures reduces the dimensionality of the dispersion and limits the number of available eigenstates. This results in a faster growth of spin wave amplitude and a more rapid onset of nonlinear scattering phenomena [27].

2.5 Yttrium Iron Garnet (YIG)

Yttrium Iron Garnet (YIG) is an insulating ferrimagnetic material notable for its exceptionally low magnetic damping (α from Equation 2.6), which enables spin wave propagation over significant distances. This minimal magnetic loss is attributed to the weak spin-orbit interaction, resulting in low magnon-phonon coupling. YIG samples are commonly grown on a Gadolinium Gallium Garnet (GGG) substrate using liquid-phase epitaxy (LPE). The closely matched lattice constants of YIG and GGG facilitate the production of high-quality, defect-free, and stress-free films. This reduction in inhomogeneities effectively minimizes two-magnon scattering, which is the elementary process whereby, at a static magnetic non-uniformity, one magnon is transformed into another magnon with the same frequency but with a different wavevector. The most efficient two-magnon scattering occurs for magnons with wavelengths close to the size of the non-uniformity [1, 28, 25].

YIG ($Y_3Fe_5O_{12}$) has a complex crystal structure, as shown in Figure 2.8. The cubic crystal structure of YIG is divided into three distinct cation sub-lattices. The five iron ions per formula unit are the only magnetic constituents and are distributed between tetrahedral and octahedral sites. The three iron ions in one sub-lattice and two in the other interact through superexchange interaction, resulting in antiparallel spin orientation. This leads to a net magnetic moment due to one iron ion per formula unit [20, 29]. The saturation magnetization of YIG at the temperature of 293 K is

$$M_\mathrm{S} = 140\,\mathrm{kA\,m^{-1}}\ \ [24].$$

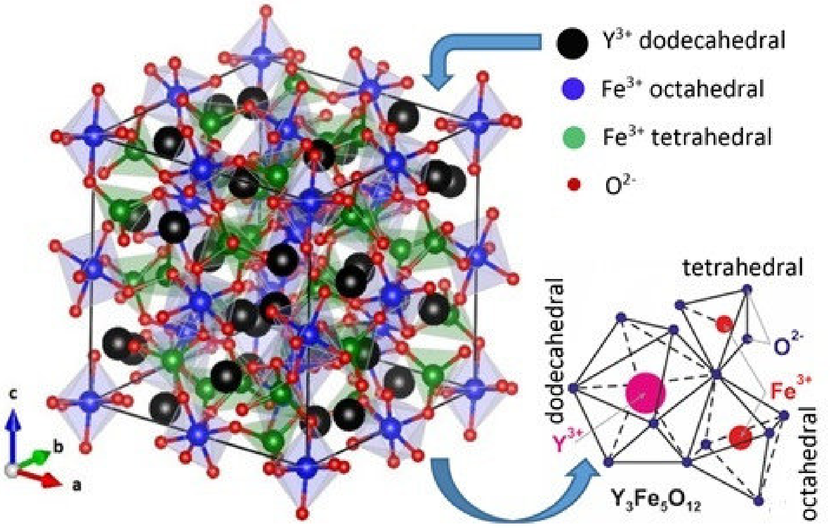

Figure 2.8: Unit cell of YIG ($Y_3Fe_5O_{12}$) with three distinct cation crystallographic sublattices (taken from [29]).

3 State of the Art - Inverse Design Magnonics

In the field of photonics inverse design is already employed for many functionalities. Using photons as data carriers inverse design-based demultiplexers [8], synapses [9], and neurons [10] based on inverse design have been developed. The adoption of inverse design in the field of magnonics has sparked a wave of new innovative research. To establish a robust foundation for this thesis on the recent use of inverse design for the development of magnonic devices, it is vital to review pioneering works in the field. In the following sections, three particularly influential papers provide essential insights into the current advancements.

3.1 Inverse-Design Magnonic Devices

The first pivotal study, “Inverse-design magnonic devices” [15] by Qi Wang, Andrii V. Chumak, and Philipp Pirro, published in Nature Communications in May 2021, introduces the method of inverse design in magnonics. Crucial for realizing functionalities through inverse design is the utilization of a design region. This design region is then optimized by a feedback-based computational algorithm to produce the desired functionality. The first functionality discussed in the study is a magnonic frequency demultiplexer. The utilized structure is displayed in Figure 3.1. It consists of one input waveguide and two output waveguides connected by the design region. The design region is divided into 10×10 elements. These elements can either be filled with the magnetic material (100 nm thick YIG) or left empty. FVMSW are used with an external out-of-plane field of 200 mT. Spin waves of two frequencies ($f_1 = 2.6\,\mathrm{GHz}$ and $f_2 = 2.8\,\mathrm{GHz}$) are then excited in the input wavequide and simulated using MuMax3, an open-source GPU-accelerated micromagnetic simulation program [30]. A direct binary search algorithm is then employed to iteratively change the design region to separate the two frequencies into the different outputs. Figure 3.2 shows the achieved results. The main mechanism responsible for generating the functionality is multi-path interference within the design region. Constructive interference results in high transmission at the desired output, while destructive interference causes the cancellation of the spin wave intensity at the other output. The transmission of frequencies f_1 and f_2 at the corresponding outputs is around 96% and 80%, respectively, with crosstalk between the two frequencies of less than 3%.

Multiple other devices, such as a magnonic multiplexer, a nonlinear switch, and a circulator, were also successfully realized using the same principles with only minor adaptations to the structure or design region.

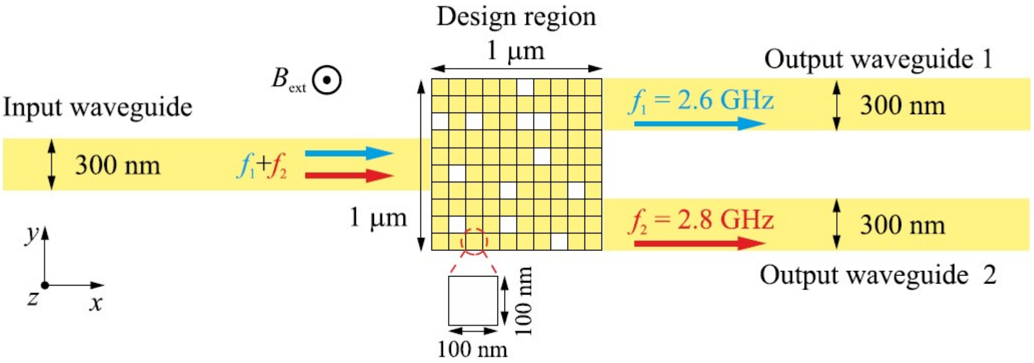

Figure 3.1: The structure utilized to realize an inverse designed frequency demultiplexer. It consists of one input waveguide and two output waveguides and a design region divided into 10×10 elements. The yellow regions indicate the magnetic material (YIG) and the white holes imply the removal of the material (taken from [15]).

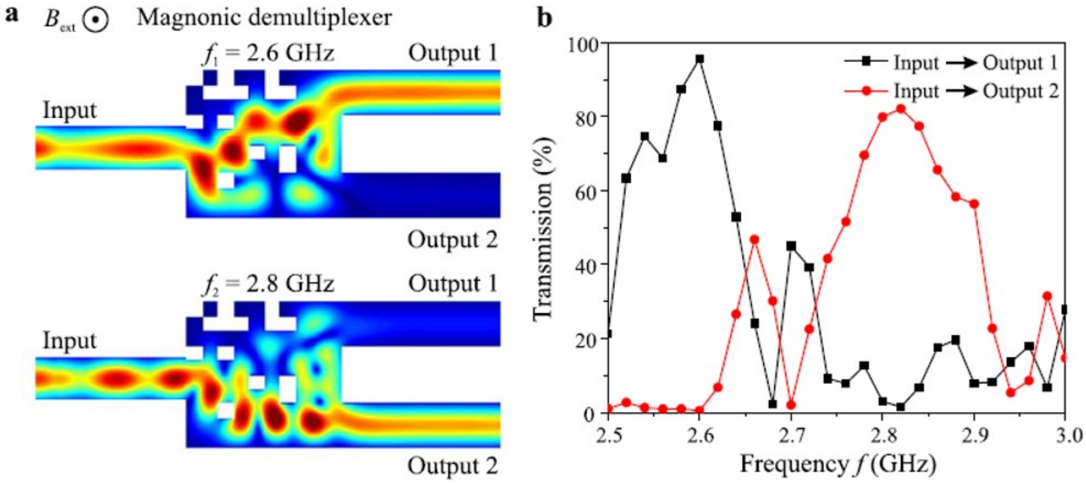

Figure 3.2: Results of the inverse designed magnonic frequency demultiplexer. (a) The normalized spin wave amplitude map shows the guidance of different frequencies to different outputs. (b) Spin wave transmission for a frequency sweep from 2.5 GHz to 3 GHz (taken from [15]).

3.2 Nanoscale Neural Network using Non-Linear Spin-Wave Interference

The second significant paper, "Nanoscale neural network using non-linear spin-wave interference" [17] by Ádám Papp, Wolfgang Porod, and Gyorgy Csaba, also published in Nature Communications in November 2021, explores the design of neural network hardware that leverages spin-wave propagation and interference for neuromorphic computing functions. Computing models for neuromorphic devices require highly interconnected systems, leading to a large number of connections, such as those required for artificial neurons. Leveraging spin waves and their propagation through a substrate enables the use of interference to facilitate all-to-all interconnections between points. This highlights the advantages of wave-based computing concepts.

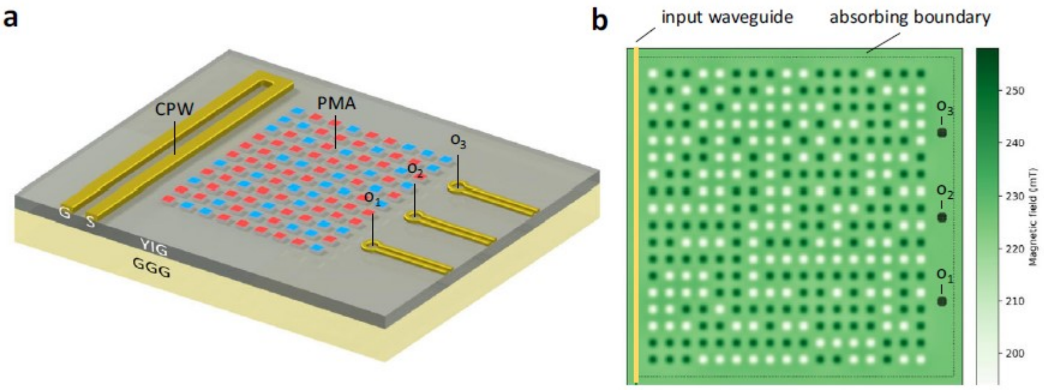

Figure 3.3: Nanomagnet-based spin-wave scatterer. (a) Schematics of the device consisting of the magnetic medium, a microwave coplanar waveguide (CPW) for spin wave excitation, multiple antennas for detection, and a punchcard-like pattern of nanomagnets. (b) The magnetic landscape generated by the nanomagnets used to create functionalities by inverse design (taken from [17]).

Figure 3.3 shows the structure of this nanomagnet-based spin wave scatterer envisioned in this study. It consists of the magnetic material (YIG on GGG), a microwave coplanar waveguide (CPW) for spin wave excitation, multiple antennas for detection, and a punchcard-like pattern of nanomagnets. These nanomagnets exhibit strong perpendicular magnetic anisotropy (PMA), with their magnetization oriented out of plane, either upwards or downwards. This results in a spatially non-uniform magnetic field acting on the spin wave medium and, consequently, creating an interference pattern. This 10 µm × 10 µm structure is simulated with a GPU-based, custom-built full micromagnetic solver based on a machine learning framework (Pytorch [31]). Instead of relying on a (nonlinear) wave equation to model the wave propagation, the volumes were discretized into 25 nm × 25 nm × 25 nm volumes and the LLG equation was used to calculate the precession of the magnetic moments. The inverse design approach is then used to find the magnetic field distribution which scatters the spin waves in the way needed to achieve the desired functionality. This micromagnetic design engine they developed was named “Spintorch” [32].

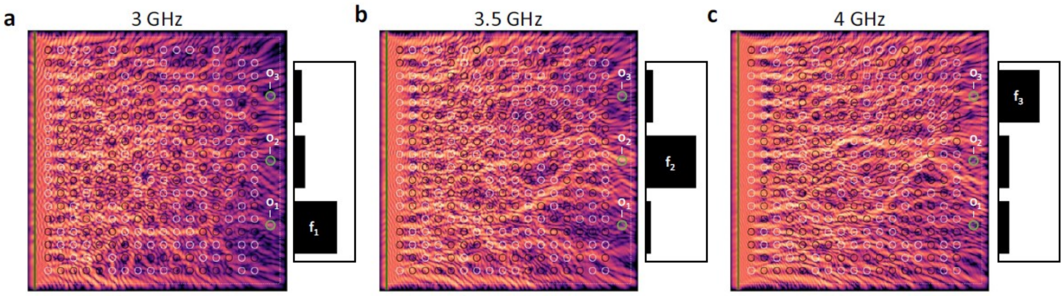

Figure 3.4: Results for the inverse designed spin wave spectrum analyzer showing the seperation of three different frequencies to three different outputs (taken from [17]).

Similar to the previously reviewed study, the first functionality presented is a spectrum analyzer. Spin waves of frequencies $f_1 = 3\,\text{GHz}$, $f_2 = 3.5\,\text{GHz}$, and $f_3 = 4\,\text{GHz}$ were used and successfully separated into three distinct outputs. The results are shown in Figure 3.4. Even with intentional switching errors in the magnet states, the inverse-designed states demonstrated considerable robustness and maintained performance.

Instead of focusing frequencies to different outputs, the device is also able to identify certain spectral patterns. This capability was demonstrated by implementing vowel recognition. Vowel samples available in the Wavetorch package [33] were scaled up to microwave frequencies. To correspond with the recognized vowels, the scatterer structure was trained to maximize spin wave intensity at one of the three output points. After training, the device was able to successfully identify the vowel samples with accuracy ranging from 60% up to 87.5%, depending on the vowel. However, additional investigations were conducted on the impact of nonlinearity when creating the functionality. By entering the nonlinear regime—achieved by increasing the excitation field from 1 mT to 50 mT—the accuracy of recognition improved to 90% to 97.5%. Although nonlinearity is not necessarily required to create these linear functionalities, introducing nonlinear effects can enhance the computational capabilities of the device. Similar to the effect of the nanomagnets, the large amplitude of the spin waves also shifts spin wave dispersion. This adds degrees of freedom, thereby increasing the capability of the device.

The final demonstrated functionality relies entirely on nonlinearity and cannot be achieved in a linear system. Two waves ($f_1 = 3\,\text{GHz}$ and $f_2 = 4\,\text{GHz}$) are directed towards the same output. Only if both waves are simultaneously present should the intensity be redirected to a second output. In the linear regime, the superposition of these two waves does not produce a different result. However, the nonlinearity of spin waves can be utilized to create this type of functionality.

3.3 Experimental Demonstration of a Spin-Wave Lens Designed with Machine Learning

The third noteworthy study, “Experimental Demonstration of a Spin-Wave Lens Designed with Machine Learning” [16] by Martina Kiechle et al., published in IEEE Magnetics Letters in September 2022, presents the design and experimental realization of a spin-wave lens created using machine learning algorithms. In this study, the variable used to design functionalities is the effective saturation magnetization M_{eff}. Experimentally, this is achieved through focused-ion-beam (FIB) irradiation. Although no material is removed by the FIB irradiation, the ion implantation causes a structural change of the YIG crystal on the nanoscale. Figure 3.5 shows the dependence of the irradiation dose on both the wavelength and effective saturation magnetization in YIG. The wavelength was determined experimentally, and the effective saturation magnetization was then calculated using the dispersion relation. It was found that the intrinsic effective magnetization, $M_{\text{eff},0} = 142.8\,\text{kA}\,\text{m}^{-1}$, can be increased up to $M_{\text{eff,max}} = 144.7\,\text{kA}\,\text{m}^{-1}$. This corresponds to spin-wave wavelengths ranging from $\lambda_0 = 5\,\mu\text{m}$ (unirradiated) down to $\lambda_{\text{FIB}} = 3\,\mu\text{m}$ for the maximum FIB dose. This variation in M_{eff}, which shifts the dispersion and changes the wavelength of the spin waves, is then utilized in a $50\,\mu\text{m} \times 50\,\mu\text{m}$ design region.

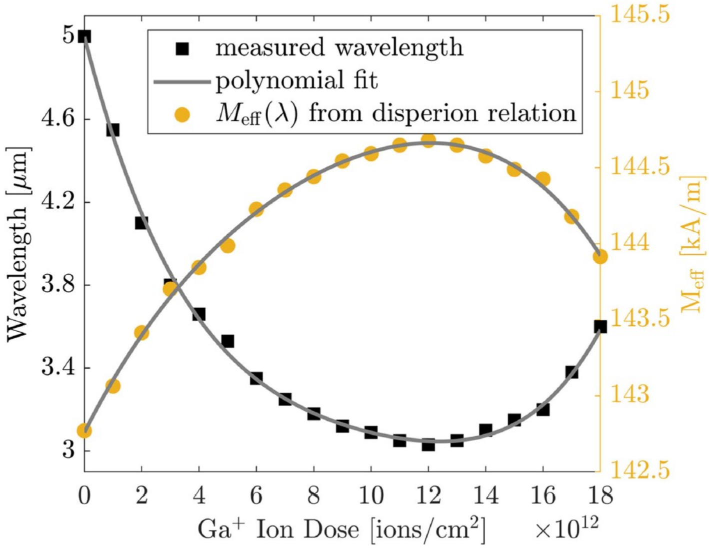

Figure 3.5: Influence of the FIB irradiation dose on the wavelength and effective saturation magnetization in YIG. The spin-wave wavelength was determined experimentally and then used to calculate the effective saturation magnetization M_{eff} by using the dispersion relation (taken from [16]).

First, Spintorch is employed to simulate the system. After finding a solution for the desired functionality, experimental verification is carried out by irradiating the pattern onto a YIG sample. A 69 nm thick YIG film with a CPW microwave antenna for excitation

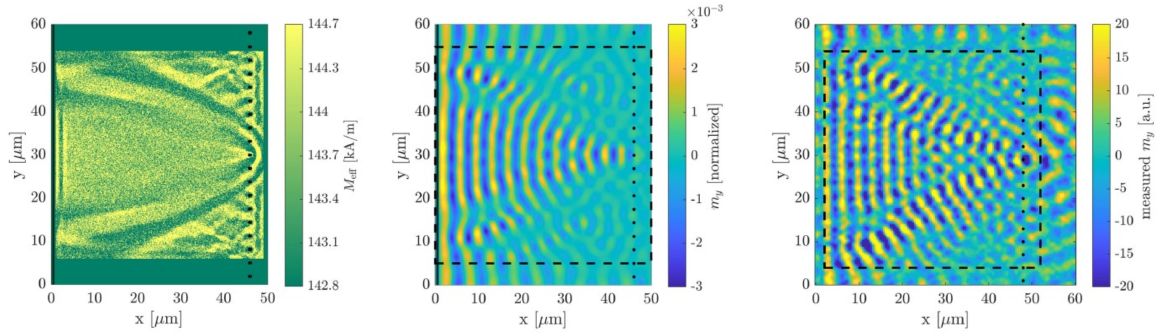

(a) (b) (c)

Figure 3.6: Inverse designed spin-wave lens focusing spin waves to the center of the structure. (a) Binary saturation magnetization map created by Spintorch. (b) Spin-wave propagation simulated in MuMax3, showing the focusing of the spin wave. (c) Experimental varification of the design by longitudinal time-resolved magnetooptical Kerr effect (trMOKE) measurements (taken from [16]).

on one side and multiple outputs on the other side is used. An out-of-plane bias field (FVMSW) of 282.5 mT is used to excite spin waves at $f = 3$ GHz. For the simulation, the area was discretized into 100 nm × 100 nm squares. Figure 3.6 shows the results for a spin-wave lens focusing spin waves to the center of the structure. Figure 3.6a shows the binary saturation magnetization map created by the inverse-design algorithm. In Figure 3.6b, the design verification using MuMax3 [30] is shown. This represents the final step before fabricating the design via FIB irradiation. Figure 3.6c shows the experimental validation of the design. Using longitudinal time-resolved magneto-optical Kerr effect (trMOKE) microscopy, a two-dimensional spin-wave pattern was recorded. The comparison indicates that the simulation results align well with the experimental data.

Another spin-wave lens, which focuses the beam to a different output, was also realized. This time, the focusing was offset. The inverse design algorithm successfully created the desired functionality, and MuMax3 simulations along with experimental verification were conducted. For the experimental verification, the focus was in the correct location, although it was not at the highest intensity. Additionally, the image showed a much noisier background. This could be due to fluctuations in the ion beam current or other imperfections in the experiment.

4 Methodology

In this chapter, the experimental setup, materials, and methods are described. The first section provides an explanation of a standard propagating spin-wave spectroscopy (PSWS) experimental setup, which forms the foundation for the developed inverse-design magnonic processor. Although the detailed description of the experimental setup is provided later, examples and calculations in this section are based on the instrumentation of the developed setup. The subsequent section will discuss the additional components, remote control, and automation of the setup.

4.1 Propagating Spin-Wave Spectroscopy (PSWS)

The standard PSWS experimental setup consists of an electromagnet including a Hall probe, a vector network analyzer (VNA), and a sample holder equipped with two microstrip antennas. Coaxial cables are used to connect the VNA to the sample holder.

The electromagnet generates the bias field necessary to saturate the sample. A signal is transmitted from the VNA through the coaxial cables to one of the antennas. The current flowing through the antenna produces Oersted magnetic fields, which excite spin waves within the sample. These spin waves propagate along the sample and, when approaching the second antenna, induce a current within it. This induced signal is then detected by the VNA and compared to the original input.

Figure 4.1 illustrates example spectra obtained via PSWS in the BVMSW configuration at 100 mT. The figure shows the transmission S_{21} in dB from port 1 to port 2 for YIG waveguides after propagation over a distance of 8 mm. The spectra are provided for several waveguide thicknesses: 4.1 µm, 7.78 µm, and 22.83 µm, each with a width of 2 mm. Thicker waveguides exhibit stronger signals and a broader bandwidth due to the combination of higher propagation speeds and a larger antenna irradiation volume.

4.1.1 Characterization of S-parameters using a Vector Network Analyzer

The two-port VNA is equipped with both an alternating current (AC) source and a receiver for each port, capable of generating and detecting microwave signals over a wide range of frequencies while maintaining phase integrity. When a signal is transmitted through port 1 with amplitude a_1, a portion of the signal is reflected (b_1) while another portion is transmitted (b_2). The VNA displays this information as ratios of the transmitted and received signals, known as S-parameters, which are represented on a decibel (dB) scale. The reflection at port 1 is given by:

$$S_{11} = 20 \log_{10} \frac{b_1}{a_1} \tag{4.1}$$

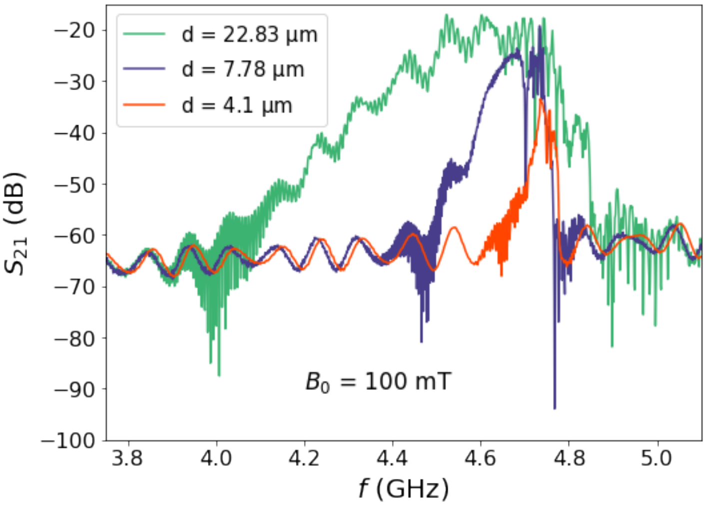

Figure 4.1: Transmission spectra for YIG waveguides of varying thicknesses (4.1 µm, 7.78 µm, 22.83 µm) measured at 100 mT.

and the transmission from Port 1 to Port 2 is:

$$S_{21} = 20 \log_{10} \frac{b_2}{a_1}. \tag{4.2}$$

Similarly, S_{12} and S_{22} represent the reflection and transmission when sending the signal from Port 2. The VNA must be calibrated for the cables used and the desired number of data points. This calibration corrects for the phase delay of the cables and ensures that impedance measurements are as accurate as possible.

4.1.2 Guidance and Transmission of Microwave Signals

Transmission lines are essential for carrying signals between circuit components and for designing passive circuits. At connection points, it is crucial to match the impedance of the components to minimize reflections at interfaces. In microwave engineering, an impedance of 50 Ω is typically used, due to a compromise between the maximum transmitted power achievable at an impedance of 30 Ω and the lowest losses at an impedance of 77 Ω. These design considerations ensure effective signal transmission and optimal system performance [34].

Coaxial Transmission Line

Coaxial transmission lines are fundamental to RF instrumentation, commonly used to interface laboratory equipment such as synthesizers, amplifiers, and antennas. The geometry of a coaxial transmission line is depicted in Figure 4.2. It consists of two concentric cylindrical conductors with inner radius r_1 and outer radius r_2, separated by a homogeneous dielectric material. The dielectric material has a relative permittivity of ϵ_r.

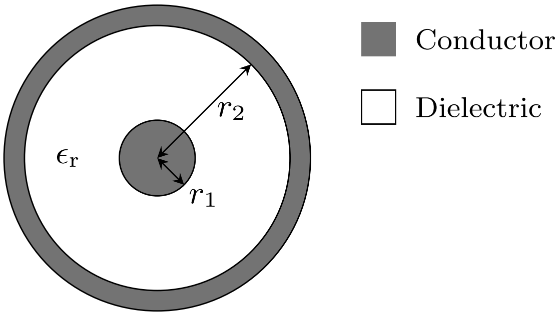

Figure 4.2: Geometry of a coaxial transmission-line with the inner radius r_1 and the outer radius r_2.

The transmission line serves as a guide for the electromagnetic wave, which propagates as a transverse electromagnetic mode (TEM) wave. In this mode, the electric and magnetic field lines are perpendicular to the direction of propagation. Beyond a certain critical frequency, higher-order modes can also propagate. The use of these specialized cables and transmission lines is crucial when working with high-frequency AC signals. This necessity arises due to the skin effect, which causes the current to flow predominantly near the surface of the conductor at high frequencies. The skin effect is illustrated in Figure 4.3 for a cylindrical conductor and can be understood with the Maxwell equations (Section 2.1). The high-frequency current flowing through the conductor induces an alternating rotational magnetic field (Equation 2.4). The time-varying magnetic field then induces a rotational electric field (Equation 2.3), resulting in circulating eddy currents.

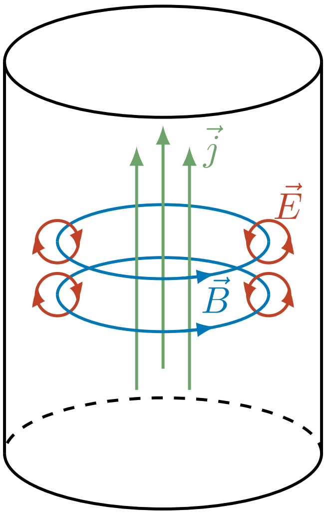

Figure 4.3: Illustration of the skin effect for a cylindrical conductor. The interactions of electric and magnetic fields results in partial cancellation of the current in the center of the conductor.

Due to their anti-parallel alignment, these eddy currents partially cancel the current flow in the center of the conductor and reinforce it near the surface [35, 34]. Considering a loss-less transmission line the characteristic impedance Z_0 of a coaxial transmission line can be calculated with the inductance per unit length L', the capacitance per unit length C' and the material parameters ϵ_r and μ_r:

$$Z_0 = \sqrt{\frac{L'}{C'}} = \frac{\mathrm{c}L'}{\sqrt{\epsilon_\mathrm{r}\mu_\mathrm{r}}}. \tag{4.3}$$

Since technical transmission lines commonly use non-magnetic, dielectric materials $\mu_\mathrm{r} = 1$. The inductance per unit length L' is obtained by

$$L' = \frac{\mu_0}{2\pi} \ln\left(\frac{r_2}{r_1}\right) \tag{4.4}$$

which results in

$$Z_0 = \sqrt{\frac{\mu_0}{\epsilon_0}} \frac{1}{\sqrt{\epsilon_\mathrm{r}}} \frac{1}{2\pi} \ln\left(\frac{r_2}{r_1}\right) \tag{4.5}$$

for the the characteristic impedance [34].

Microstrip Transmission Line

In the PSWS setup, the microstrip transmission lines connect to the coaxial cables. At this junction, it is important to match the impedance of the components, which determines the width of the microstrip. The microstrip is then continuously and smoothly tapered in width down to 50 µm. At this point, it functions as a microstrip antenna used for spin-wave excitation. The generated alternating Oersted field around the antenna initiates the spin precession. This radiating part is also referred to as the transducer [34].

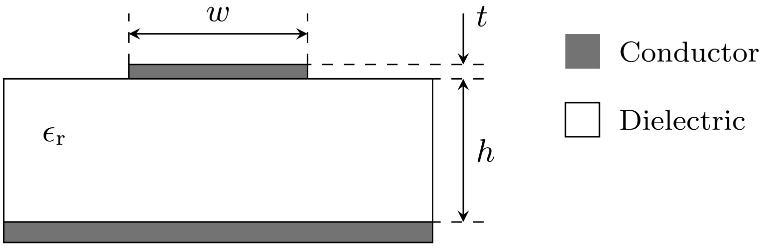

Figure 4.4: Geometry of a microstrip transmission line, showing the substrate height h, microstrip width w, and microstrip thickness t.

Figure 4.4 shows the geometry of a microstrip line with the substrate height h, the microstrip width w, and the microstrip thickness t. It is very similar to the geometry of the coaxial lines discussed in the previous section. The coaxial line can be imagined as a rolled-up microstrip. It consists of two electrical conductors: the continuous ground plane and a small rectangular line. These two metallic parts are separated by a dielectric insulator. When an electromagnetic wave propagates on the microstrip, it propagates partially in the air above the microstrip and partially in the substrate between the strip and the ground plane. In this case, the fundamental wave mode is called quasi-TEM. This is due to the small longitudinal electric and magnetic field components at the boundary of the air and the substrate [34].

To calculate the impedance of a microstrip line, an effective dielectric constant ϵ_{eff} is first introduced. This accounts for the fact that the electromagnetic wave propagates through both the air above the microstrip and the dielectric material beneath it. The effective dielectric constant represents a new, homogeneous medium. The formula for ϵ_{eff} is

$$\epsilon_{\text{eff}} = \frac{\epsilon_{\text{r}} + 1}{2} + \frac{\epsilon_{\text{r}} - 1}{2} \frac{1}{\sqrt{1 + \dfrac{12h}{w}}}. \tag{4.6}$$

Once ϵ_{eff} is determined, the characteristic impedance Z_0 of the microstrip line can be approximated using the following equations:

$$Z_0 = \begin{cases} \dfrac{60}{\sqrt{\epsilon_{\text{eff}}}} \cdot \ln\left(\dfrac{8t}{w} + \dfrac{w}{4h}\right) & \text{for } \dfrac{w}{h} \leq 1 \\ \dfrac{120\pi}{\sqrt{\epsilon_{\text{eff}}}\left(\dfrac{w}{h} + 1.393 + 0.667 \cdot \ln\left(\dfrac{w}{h} + 1.444\right)\right)} & \text{for } \dfrac{w}{h} \geq 1 \text{ [36].} \end{cases} \tag{4.7}$$

A duroid substrate with a height of $h = 254\,\mu\text{m}$ and a dielectric constant of $\epsilon_{\text{r}} = 10.2$ is used in the experiment. Figure 4.5 shows the relationship between the width of the transmission line and the characteristic impedance. This leads to a trace width of $w = 236\,\mu\text{m}$, which ensures that the transmission line impedance matches the $50\,\Omega$ standard of the remaining laboratory equipment.

4.1.3 Spin Wave Excitation and Detection

The end of the microstrip transmission line functions as the transducer for spin-wave excitation. The width is reduced to $50\,\mu\text{m}$, which broadens the excitation spectrum to cover a wider range of wavenumbers. Additionally, the end is shorted to the ground plane, which increases coupling to the magnetic medium by concentrating the current density in the microstrip [20]. To analyze spin-wave excitation, the magnetic field generated by the antenna can be approximated under a few assumptions: the high-frequency field is considered to have the same strength as the static field for a given current density j, and a homogeneous current distribution is assumed. A Cartesian coordinate system is employed (see Figure 4.6), with conductor dimensions of $2a$ and $2b$. The analysis focuses solely on the field within the xy-plane. Consequently, the current is perpendicular to the radial distance r, simplifying the Biot-Savart law (Equation 2.5) to [37]:

$$dH(X, Y) = \frac{I dx dy}{8\pi ab\sqrt{(x - X)^2 + (y - Y)^2}} \tag{4.8}$$

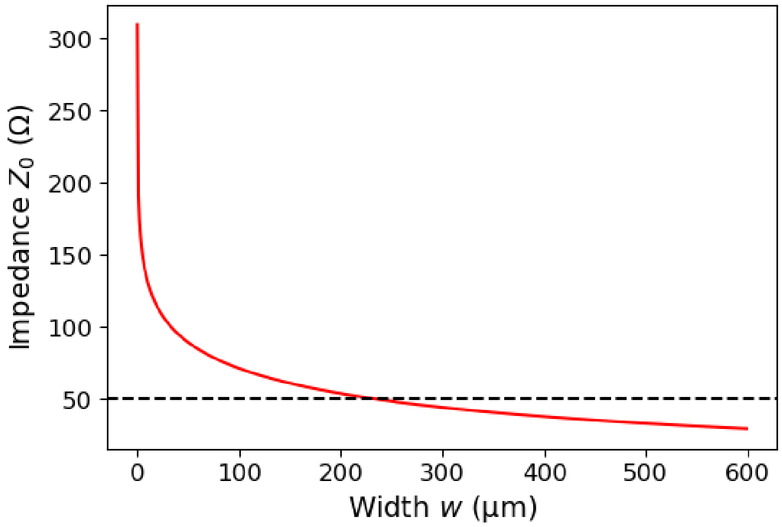

Figure 4.5: Relationship between the microstrip line width w and the characteristic impedance Z_0 for a duroid substrate with a height of $h = 254\,\mu\text{m}$ and a dielectric constant of $\epsilon_\text{r} = 10.2$.

By integrating over the antenna's area, the x and y components of the magnetic field can be determined (see full derivation in [37]):

$$\begin{aligned} H_x(X,Y) = \frac{-I}{8\pi ab}\Bigg[&(a-X)\left(\frac{1}{2}\ln\left(\frac{(b-Y)^2+(a-X)^2}{(-b-Y)^2+(a-X)^2}\right)+\frac{b-Y}{a-X}\arctan\left(\frac{a-X}{b-Y}\right)\right.\\ &\left.-\frac{-b-Y}{a-X}\arctan\left(\frac{a-X}{-b-Y}\right)\right)-(-a-X)\left(\frac{1}{2}\ln\left(\frac{(b-Y)^2+(-a-X)^2}{(-a-X)^2+(-b-Y)^2}\right)\right.\\ &\left.+\frac{b-Y}{-a-X}\arctan\left(\frac{-a-X}{b-Y}\right)-\frac{-b-Y}{-a-X}\arctan\left(\frac{-a-X}{-b-Y}\right)\right)\Bigg] \end{aligned} \tag{4.9}$$

$$\begin{aligned} H_y(X,Y) = \frac{I}{8\pi ab}\Bigg[&(b-Y)\left(\frac{1}{2}\ln\left(\frac{(b-Y)^2+(a-X)^2}{(-a-X)^2+(b-Y)^2}\right)+\frac{a-X}{b-Y}\arctan\left(\frac{b-Y}{a-X}\right)\right.\\ &\left.-\frac{-a-X}{b-Y}\arctan\left(\frac{b-Y}{-a-X}\right)\right)-(-b-Y)\left(\frac{1}{2}\ln\left(\frac{(a-X)^2+(-b-Y)^2}{(-a-X)^2+(-b-Y)^2}\right)\right.\\ &\left.+\frac{a-X}{-b-Y}\arctan\left(\frac{-b-Y}{a-X}\right)-\frac{-a-X}{-b-Y}\arctan\left(\frac{-b-Y}{-a-X}\right)\right)\Bigg]. \end{aligned} \tag{4.10}$$

The antenna width of 50 µm and a thickness of 18 µm results in $a = 25\,\mu\text{m}$ and $b = 9\,\mu\text{m}$. For the current a simplified estimation can be made with the resistance of a conductor

$$R = \frac{\rho l}{A}, \tag{4.11}$$

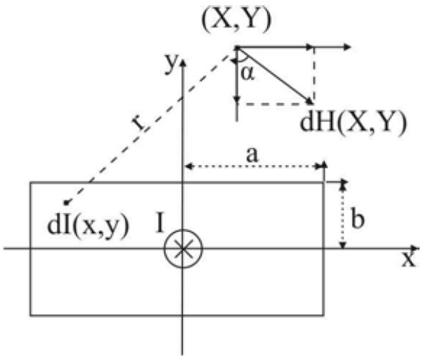

Figure 4.6: Coordinate system for calculation of the antenna field (taken from [37]).

the antenna length of $l = 1.3\,\mathrm{mm}$, the antenna cross-sectional area $A = 4ab$ and the resistivity of copper $\rho = 1.68 \cdot 10^{-8}\,\Omega\,\mathrm{m}$. Furthermore, using the simple equation for electrical power

$$P = RI^2, \tag{4.12}$$

at a power of 1 mW the current

$$I = \sqrt{\frac{PA}{\rho l}} = 203\,\mathrm{mA}$$

can be calculated.

The magnetic field of the antenna, calculated using equations 4.9 and 4.10, is illustrated in Figure 4.7. For FVMSW, the $H_x(x, y)$ component is relevant for spin wave excitation, as it directly initiates spin precession due to its orthogonality to the magnetic moment. Contrarily, the $H_y(x, y)$ component is parallel (or antiparallel) to the sample's magnetization and does not contribute to initiating spin precession. Although small z-components of the magnetic field in the quasi-TEM mode could also contribute, they are neglected in this approximation. Figure 4.8a shows the $H_x(x, y)$ component at a fixed y value near the surface of the YIG film, as indicated by the dashed red line in Figure 4.7. The excitation efficiency, which depends on the wavenumber k, is given by the Fourier transform of $H_x(x, y)$ [38]:

$$\hat{H}_x(k_x) = \int_{-\infty}^{\infty} H_x(x, y)\mathrm{e}^{\mathrm{i}k_x x}\,\mathrm{d}x \tag{4.13}$$

The normalized Fourier transform is depicted in Figure 4.8b and shows which wavevectors k can be excited by the microstrips. Calculated at $y = -10\,\mu\mathrm{m}$ with integration limits of $\pm 0.5\,\mathrm{mm}$. The excitation spectrum of the microstrip is related to its width; a smaller width results in a broader excitation spectrum, extending to higher k waves.

The reverse process, where propagating spin waves induce a magnetic field that generates currents within the antenna, operates on similar principles. Consequently, the excitation efficiency shown in Figure 4.8b also reflects the detection efficiency of the antenna.

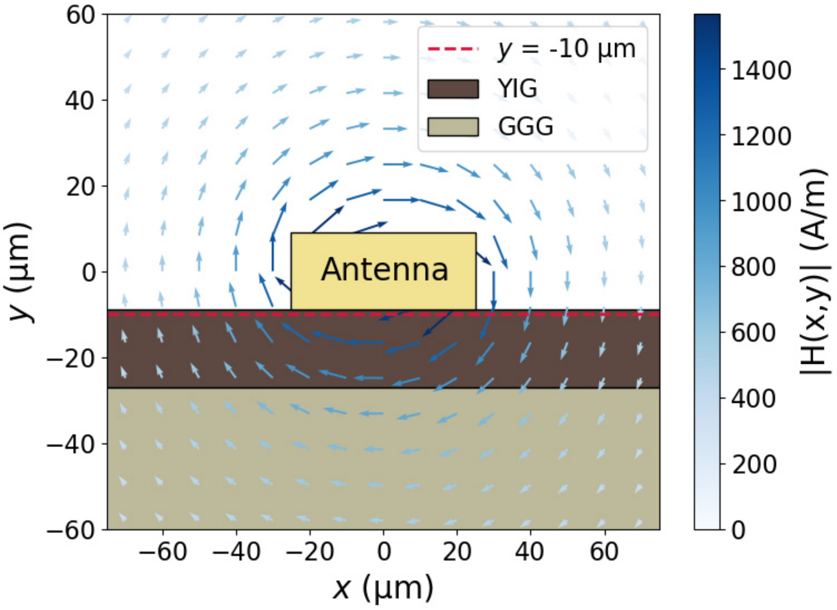

Figure 4.7: Magnetic field generated by the microstrip antenna. Red dashed line indicates $y = -10\,\mu\mathrm{m}$ near the surface of the YIG film.

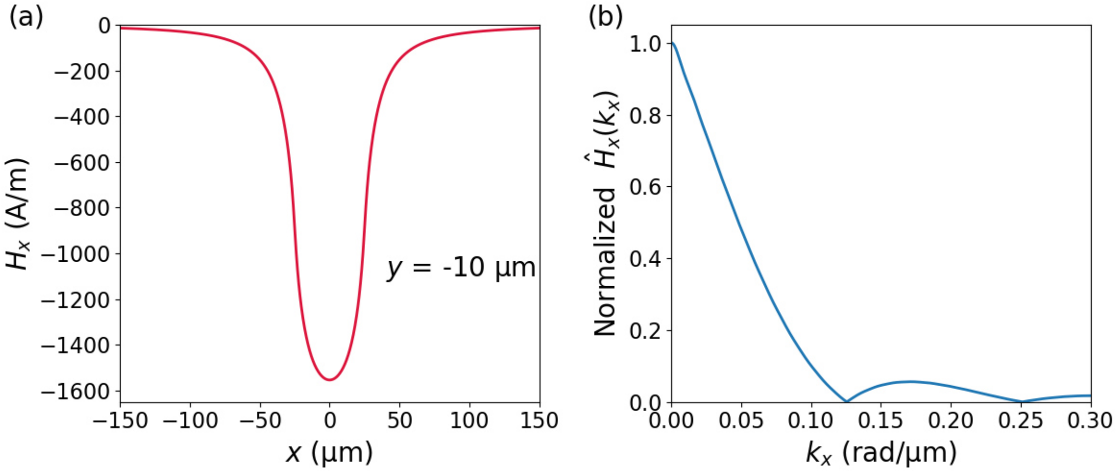

Figure 4.8: (a) Magnetic field component $H_x(x, y = -10\,\mu\mathrm{m})$, generated by the antenna, relevant for spin-wave excitation (see the red dashed line in Figure 4.7). (b) Normalized Fourier transform of $H_x(x, y = -10\,\mu\mathrm{m})$ showing the available spin-wave excitation spectrum.

4.2 Inverse Design Experimental Setup

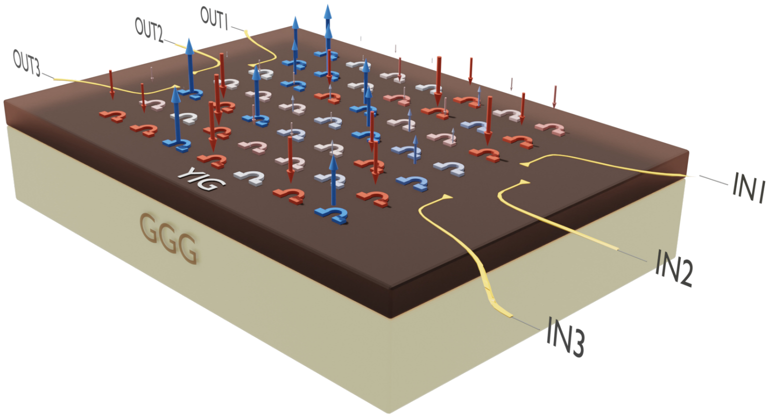

Figure 4.9: Inverse-design magnonic processor featuring a 7×7 omega-shaped DC loop array, three input, and three output spin-wave transducers on top of an 18 µm-thick YIG film.

The experimental inverse design magnonic device is depicted in Figure 4.9. It employs an 18 µm-thick YIG film with a rectangular shape of 24 mm × 17.5 mm, grown on a 500 µm GGG substrate via LPE. This relatively thick sample was selected to optimize spin-wave transport across the 2.2 cm distance between the antennas. To enhance device functionality, three input and three output spin-wave transducers have been integrated. The most vital component, making the inverse-design process experimentally possible, is a printed circuit board (PCB) comprising a 7×7 omega-shaped DC loop array. This setup also includes a multi-channel current source, developed by Elbatech Srl., capable of applying currents in the range of ±1 A for each channel. These current loops generate magnetic fields parallel or antiparallel to the out-of-plane bias field, influencing spin wave propagation dynamics. The PCB is separated from the YIG film by an insulating Teflon layer of 50 µm thickness, which prevents spin wave scattering by the metallic loops and acts as a barrier to prevent heat transfer between the loops and the YIG.

The remaining setup consists of the Anritsu MS4642B VNA, rated from 10 MHz up to 20 GHz, which generates the microwave signal. A water-cooled electromagnet provides the bias field, controlled by a Kepco BOP20-20DL current source, and a LakeShare F41 Teslameter. A microwave Agilent 87106B coaxial switch is used to switch between inputs and outputs. Additionally, a PC is employed to enable remote control and automation of the setup.

For the achieved results, a bias field of 350 mT was set, allowing the device to operate with propagating spin waves across a frequency range of 4.9 GHz to 5.5 GHz. A reference spin-wave spectrum is shown in Figure 4.10a without any influence of the omega loops.

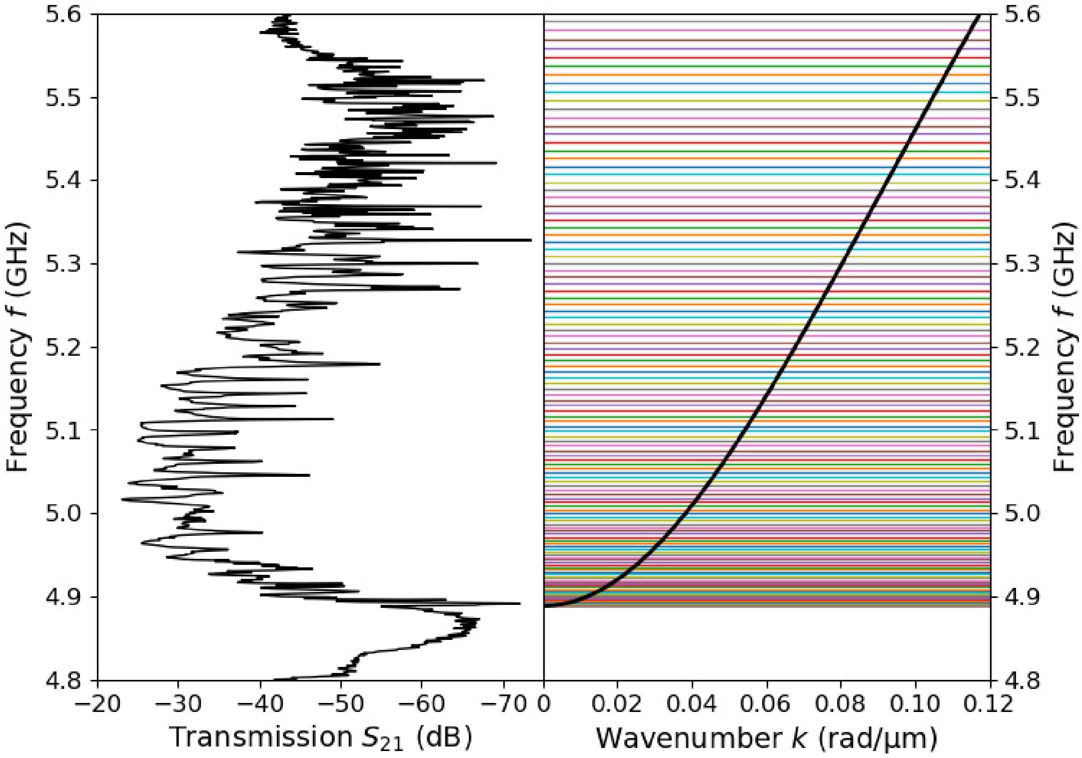

Figure 4.10: Left: Reference transmission spectrum (S_{21}^{ref} as a function of frequency) of the 18 µm-thick YIG film. Right: Dispersion relation of FVMSW for the YIG sample, highlighting the fundamental mode with a bold curve and PSSWs with horizontal lines.

Insertion losses of 25 dB can be observed, which are attributed to damping losses in spin-wave propagation and the relatively low efficiency of excitation and detection. Figure 4.10b shows a more sophisticated calculation of the spin-wave dispersion for the actual sample shape. Most importantly it takes into account the hybridization of the FVMSW mode with perpendicular standing spin wave (PSSW) modes. The fundamental mode is highlighted by the bold curve. The hybridization of these modes causes low-transmission regions in the spin-wave spectrum [39, 40]. The analysis of the fundamental FVMSW mode dispersion curve alongside the transmission S_{21} spectrum shows that the spin-wave wavelength working region spans from about $\lambda = 2\pi/k = 10\,\mathrm{mm}$ to $\lambda = 50\,\mu\mathrm{m}$.

Figure 4.11 presents systematic measurements of the transmission S_{21} from each input IN_i to each output OUT_j of the assembled setup at a magnetic field of 350 mT. This includes the 18 µm-thick YIG sample with the insulating Teflon layer and PCB placed on top, as well as the coaxial switch.

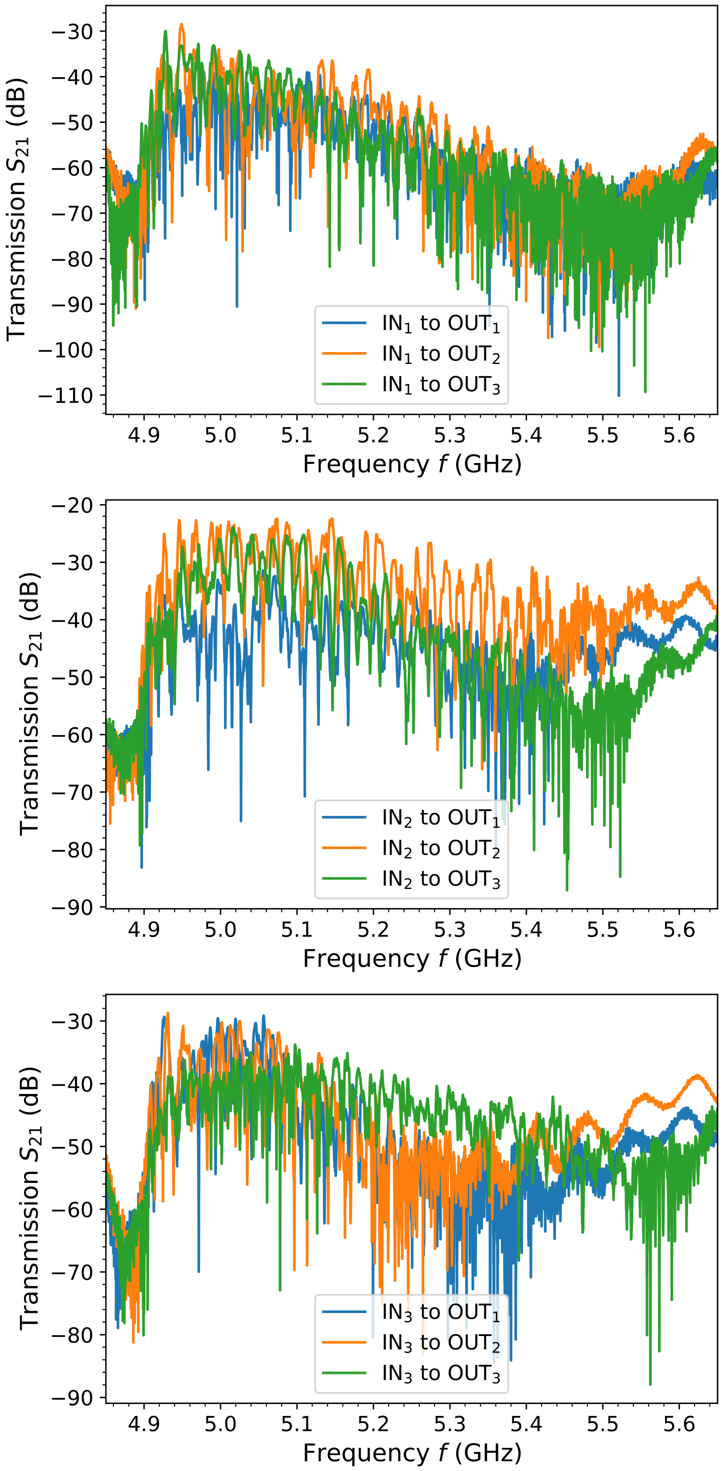

Figure 4.11: Transmission S_{21} from each input IN_i to each output OUT_j of the fully assembled setup at a magnetic field of 350 mT.

4.2.1 Printed Circuit Board (PCB)

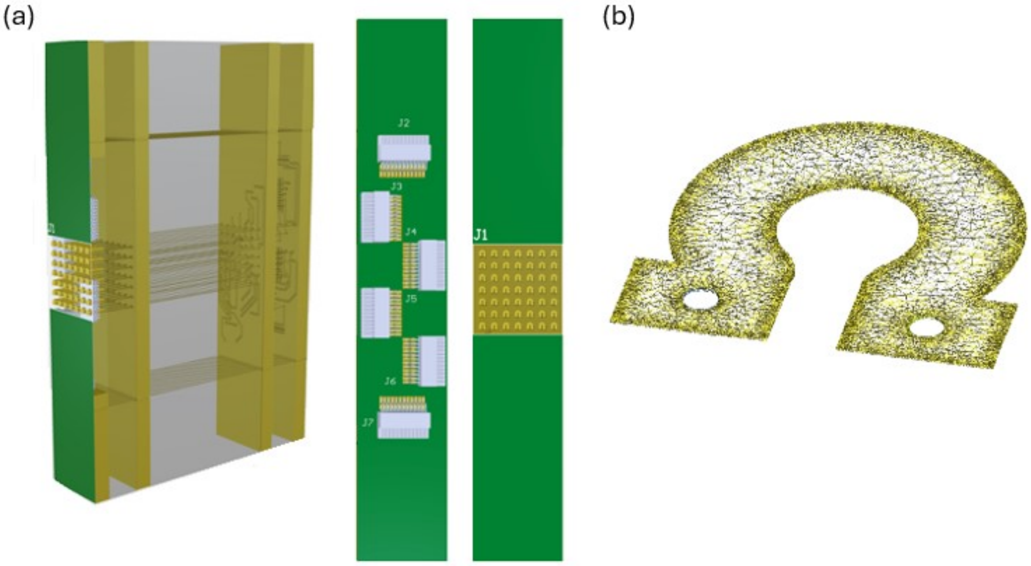

Figure 4.12: (a) Design of the PCB which functions as the design region for the magnonic inverse-design device. It generates a magnetic landscape which creates complex scattering of spin waves to achieve a desired functionality. (b) Mesh of an individual omega-shaped current loop used for simulation of the generated magnetic field.

The core element of the experimental setup is the PCB, which generates a magnetic landscape that induces complex scattering behavior in spin wave propagation, thereby enabling the inverse design process to realize various functionalities. Figure 4.12 illustrates the PCB design. Figure 4.12a shows the four metallic PCB layers with connections through vias, highlighting the front with the 7×7 omega-shaped DC loop array and the back with the soldered connectors that link the loops to the current sources. Figure 4.12b displays the geometry of an individual omega loop. The inner radius of the loop is 0.2 mm and the outer radius 0.5 mm. The center-to-center distance between loops is 2 mm, and the material used is copper with a thickness of 9 µm. The mesh depicted in Figure 4.12b, along with the Teflon, YIG, and GGG layers, was utilized to simulate the magnetic field generated inside the YIG film using Magnum.pi. Magnum.pi is a finite-element micromagnetic simulation software [41]. The simulated magnetic field of an individual loop, when a current of $-300\,\mathrm{mA}$ is applied, is displayed in Figure 4.13. The field distribution of this simulation is further analyzed in Figure 4.14a. It shows each component of the magnetic field along the y-axis (in-plane along the cross-section in Figure 4.13) at the surface of the YIG film. A new parameter, $a = 0.531\,\mathrm{mm}$, is introduced here. This parameter represents the full width at half maximum (FWHM) of the out-of-plane magnetic field and indicates the area of influence exerted by the loops. Figure 4.14b shows the out-of-plane magnetic field strength at the center of the loop on the YIG surface as a function of the electric current I through the loop. The omega loops can generate a magnetic field of approximately ±5 mT when a current of up to ±1 A is applied.

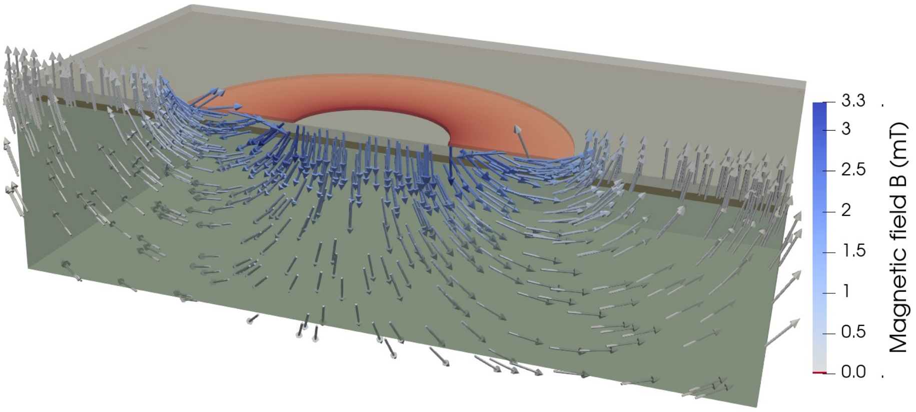

Figure 4.13: The magnetic field generated by one omega loop at a current of −300 mA. Simulated by magnum.pi, a finite-element micromagnetic simulation software [41].

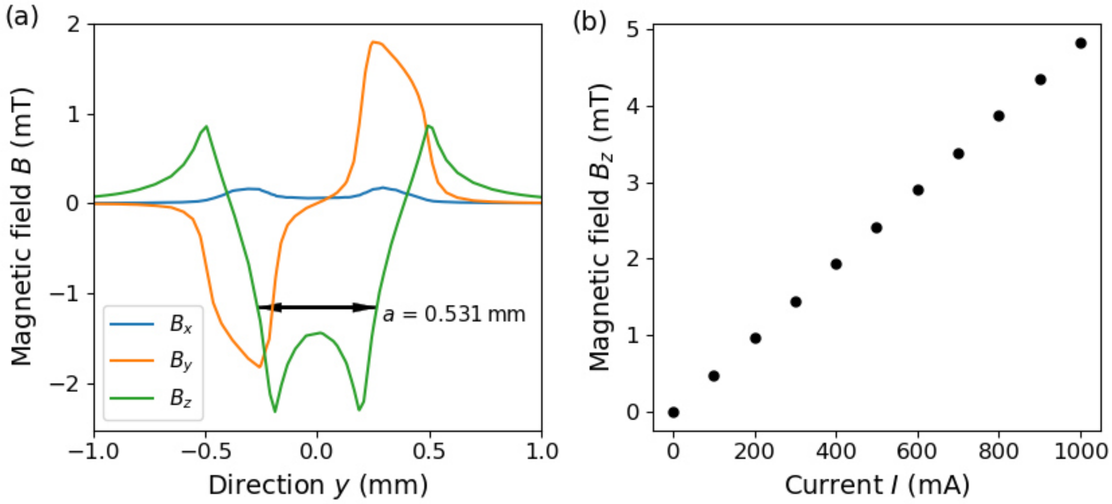

Figure 4.14: (a) Magnetic field components generated by one loop at a current of −300 mA as a function of the y direction, with the origin at the center of the omega loop. (b) Out-of-plane magnetic field B_z generated by one loop as a function of applied current I at the center of the loop at the YIG surface.

4.2.2 Multichannel Current Sources

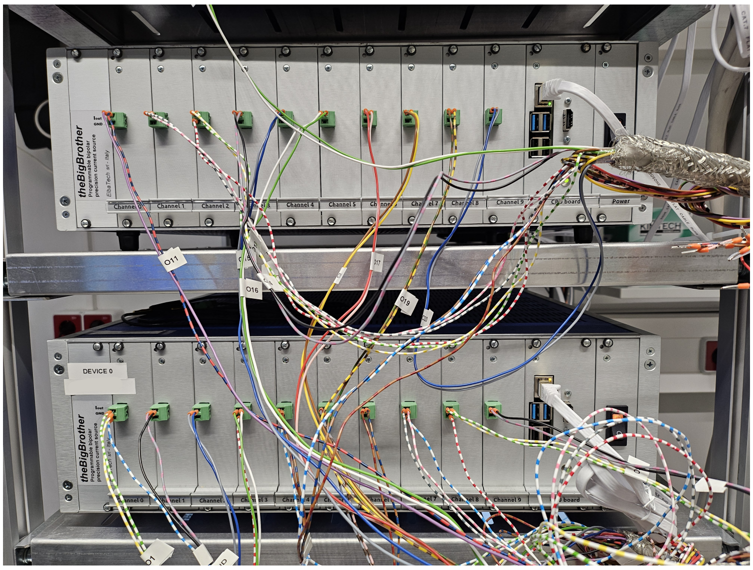

Figure 4.15: Multichannel current sources, each with 10 individually controllable channels and multiple interfaces (Ethernet, USB, HDMI). Five devices provide a total of 50 channels, with 49 connected to the PCB, applying currents in the range of ±1 A.

Figure 4.15 displays two of the multichannel current sources used in the setup. Each device is equipped with 10 individual channels and multiple interfaces, including Ethernet, USB, and HDMI, for remote control. In total, five devices are utilized, providing 50 channels. Of these, 49 are connected to the current loops via the PCB. Each channel can apply currents in the range of ±1 A with 2048 discrete steps, resulting in approximately 10^{162} degrees of freedom.

Initially, inaccuracies of ±8 mA were observed. This was later improved by implementing a feedback loop during current application, reducing the inaccuracy to ±3 mA. This limitation is due to the stability of the current channels and cannot be further improved through software adjustments, effectively reducing the degrees of freedom to approximately 10^{123}.

4.2.3 Coaxial Switch

A multiport coaxial switch is employed to switch between input and output antennas, as the VNA has only two ports. The Agilent 87106B coaxial switch, which operates up to 20 GHz, covers the entire frequency range of the VNA and is depicted in 4.16a. It features an exceptionally low insertion loss of 0.03 dB, minimal reflection, and high isolation between ports, typically greater than 100 dB up to 12 GHz and greater than 90 dB up to 20 GHz. The switch has multiple pins on the back for control purposes. Two

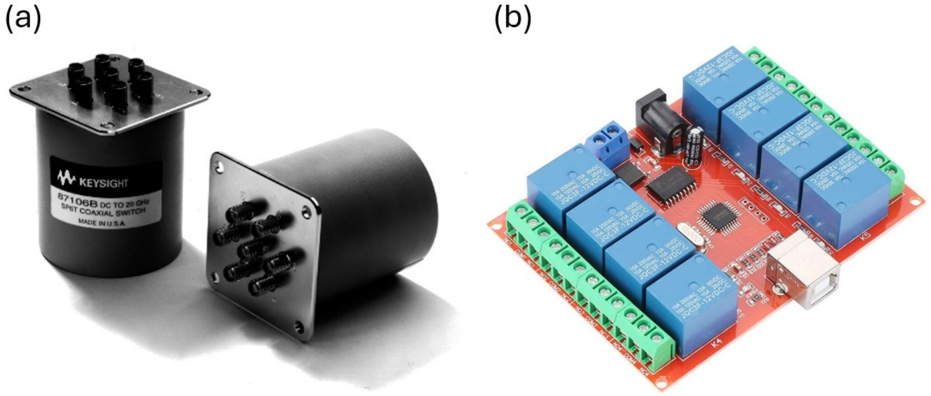

Figure 4.16: (a) Agilent 87106B coaxial switch for switching between input and output antennas. (b) Walfront USB Relay used to drive the switch pins enabling remote control.

of these pins serve as the supply (20 V to 32 V DC) and ground connections, which are directly linked to a current source. The remaining pins are designated as “drive” pins. To switch between ports, the supply is connected to one of the drive pins, causing the switch to magnetically latch and remain latched even after the source is disconnected. Since the switch lacks built-in control logic, a Walfront USB Relay (Figure 4.16b) is also used in the setup to enable remote switching control by driving the pins. The relay has a capacity of AC 250 V, 10 A and DC 30 V, 10 A for each of the eight channels, and features a Type-B USB interface for communication with a PC.

4.2.4 Remote Control

Standard Commands for Programmable Instruments (SCPI) and PyVISA

Python was utilized for the remote control and automation of the experimental setup, taking full advantage of its robust object-oriented programming capabilities. This approach enabled the creation of structured drivers for all devices, enhancing the intuitiveness and efficiency of device control. By using classes, the functionality of each device could be integrated, allowing for easy loading and intuitive interaction through class methods rather than raw commands.

For communication with most devices, the standard commands for programmable instruments (SCPI) protocol was used. SCPI is a standard for syntax and commands that allows control of test and measurement devices [42]. While SCPI offers a standardized set of commands for various devices, working with these commands directly can be complex and error-prone. Employing Python classes to handle SCPI commands makes device control more efficient and reduces the potential for errors.

To facilitate this, PyVISA [43] was employed. PyVISA is a Python package that simplifies the control of various measurement devices, independent of the interface type (e.g. GPIB, RS232, USB, Ethernet). An example of its simplicity shows that reading the self-identification of a Keithley Multimeter with GPIB number 12 requires just a few lines of code (see Listing 4.1). This example demonstrates how to list available resources, connect to the device, and communicate with it. There are three primary methods for communication: "read", which retrieves data from the device; "write", which sends commands to the device; and "query", which both sends a command and retrieves the response.

```
import pyvisa
rm = pyvisa.ResourceManager()
rm.list_resources()
('ASRL1::INSTR', 'ASRL2::INSTR', 'GPIB0::12::INSTR')
inst = rm.open_resource('GPIB0::12::INSTR')
print(inst.query("*IDN?"))
```

Listing 4.1: PyVISA example: Reading self-identification from a Keithley Multimeter with GPIB number 12 [43].

The Virtual Instrument Software Architecture (VISA) specification, established in the mid-1990s, standardizes the configuration and programming of instrumentation systems across various interfaces. It is supported by major operating systems and multiple vendors. VISA can be used with languages like Visual Basic, C, and LabVIEW. Python, through PyVISA, can interact with VISA libraries and directly access most bus systems [43].

As an example Listing 4.2 shows the developed driver to perform frequency sweep measurements with the Anritsu MS4642B VNA.

```
import pyvisa as visa
import numpy as np
import re
import time
from . import logging

def info(msg):
    logging.info_green(f"AnritsuMS4642B: {msg}")

def converter(raw):
    values = []
    pattern = r'-?\d+\.\d+E[+-]\d+'
    for line in raw.strip().split('\n'):
        match = re.search(pattern, line)
        if match:
            values.append(float(match.group()))
    return values

class AnritsuMS4642B(object):
    def __init__(self, **options):
        self._options = {
                'ip': '000.000.0.0'
        }
        self._options.update(options)
        # setup default config
        self._config = {
            'f_start': 5,    # Sweep start freq in GHz
```

```
            'f_stop': 6,  # Sweep stop freq in GHz
            'N_points': 10001, # No of measurements
            'aver': "OFF",
            'aver_typ': 'SWE',  #Per point (POIN) or per sweep (SWE)
            'N_aver': 20,   # No of points to average (1 to 1024)
            'P': 0,
            'IFBW': "500kHz"#, # IFBW, allowed values: 1, 3, 10, 30, 100, 300 Hz/ 1, 3, 10, 30, 100, 300 kHz/ 1 MHz
        }

        rm = visa.ResourceManager()
        self.instrument = rm.open_resource(f"TCPIP::{self._options['ip']}::INSTR", timeout=1000000000)
        idn = self.instrument.query("*IDN?").strip()
        info(f"Connected to device (IDN: '{idn}')")

    def config(self, **options):
        self._config.update(options)
        self.instrument.baud_rate = 115200
        self.instrument.write(f"SENS1:FREQ:STAR {self._config['f_start']:g}GHz")
        self.instrument.write(f"SENS1:FREQ:STOP {self._config['f_stop']:g}GHz")
        self.instrument.write(f"SENS1:SWE:POIN {self._config['N_points']}")
        self.instrument.write("SENS1:SWE:TYPE LIN")
        self.instrument.write("SENS1:BWID {self._config['IFBW']}")
        self.instrument.write(f"SENS1:AVER {self._config['aver']}")
        self.instrument.write("SENS1:AVER:TYP {self.config['aver_typ']}") # POIN or SWE
        self.instrument.write(f"SENS1:AVER:COUN {self._config['N_aver']}")
        self.instrument.write(f"SOUR1:POW:PORT1 {self._config['P']}dBm")
        self.instrument.write(f"SOUR1:POW:PORT2 {self._config['P']}dBm")
        self.instrument.write("CALC1:SMO OFF")
        self.instrument.write(":FORM:DATA ASC")
        self.instrument.write("LANG NATIVE")
        self._freqs = self.instrument.query_ascii_values('SENS1:FREQ:DATA?', converter = converter)[0]

    def measure(self):
        # perform the actual measurement
        info("Start measurement")
        self.instrument.write('SENS1:HOLD:FUNC HOLD')
        self.instrument.write("CALC1:PAR1:DEF S11")
        self.instrument.write("CALC1:PAR2:DEF S12")
        self.instrument.write("CALC1:PAR3:DEF S21")
        self.instrument.write("CALC1:PAR4:DEF S22")
        self.instrument.write("CALC1:PAR1:FORM MLOG")
        self.instrument.write("CALC1:PAR2:FORM MLOG")
        self.instrument.write("CALC1:PAR3:FORM MLOG")
        self.instrument.write("CALC1:PAR4:FORM MLOG")

```

```python
        self.instrument.write('SENS1:HOLD:FUNC SING')
        info("Measurement finished")

        # rescale traces
        self.instrument.write('DISP:WIND1:TRAC1:Y:AUTO')
        self.instrument.write('DISP:WIND1:TRAC2:Y:AUTO')
        self.instrument.write('DISP:WIND1:TRAC3:Y:AUTO')
        self.instrument.write('DISP:WIND1:TRAC4:Y:AUTO')

        # save data
        data = np.zeros((5, len(self._freqs)))
        data[0,:] = self._freqs
        for i in range(4):
            info(f"receive data for trace {i}")
            self.instrument.write(f"CALC1:PAR{i+1}:SEL")
            data[i+1,:] = self.instrument.query_ascii_values('CALC1:DATA:FDAT?', converter = converter)[0]

        return data
```

Listing 4.2: Anritsu MS4642B VNA Driver with PyVISA Python package.

It illustrates the class structure used for the device drivers, which includes methods for configuring and operating the device via SCPI commands after initialization. Listing 4.3 demonstrates the ease of working with these class-structured drivers. After importing the developed driver library called “maglab”, the VNA is initialized by calling the AnritsuMS4642B class. Once the device settings—such as start and stop frequency and the number of points for the sweep—are configured, the measure method can be called to obtain the S-parameters from the VNA.

```python
import maglab as ml

vna = ml.AnritsuMS4642B()
vna.config(
    f_start  = 4.8,
    f_stop   = 5.8,
    N_points = 10001,
    P = 0,
    IFBW = "10kHz"
    )
data = vna.measure()
```

Listing 4.3: Driver usage example shows the simplicity when working with class structured device drivers.

Following the same principle, drivers were created for the remaining devices to facilitate control of the Kepco current source, monitor the field using the teslameter for bias field stabilization, switch between ports via the microwave switch, and adjust the currents of the 49 individual current sources connected to the omega loops.

Magnetic Field Stabilization

The Kepco BOP20-20DL current source, which controls the electromagnet, can be operated in either voltage mode or current mode. For stabilizing the magnetic field, it is advantageous to use current mode, as it enhances the system's responsiveness. In voltage mode, commanding changes results in a slow rise or fall in current due to the coil's inductance opposing changes in current. However, in current mode, the device reaches the desired field more quickly when maintaining a stable current. This is illustrated in Figure 4.17, where a change from 3.73 V to 3.78 V in voltage mode and a change from 4 A to 4.05 A in current mode both start from and achieve approximately the same magnetic field. The increased responsiveness of current mode is clearly demonstrated, with stabilization taking more than 3 s in voltage mode and approximately 1 s in current mode.

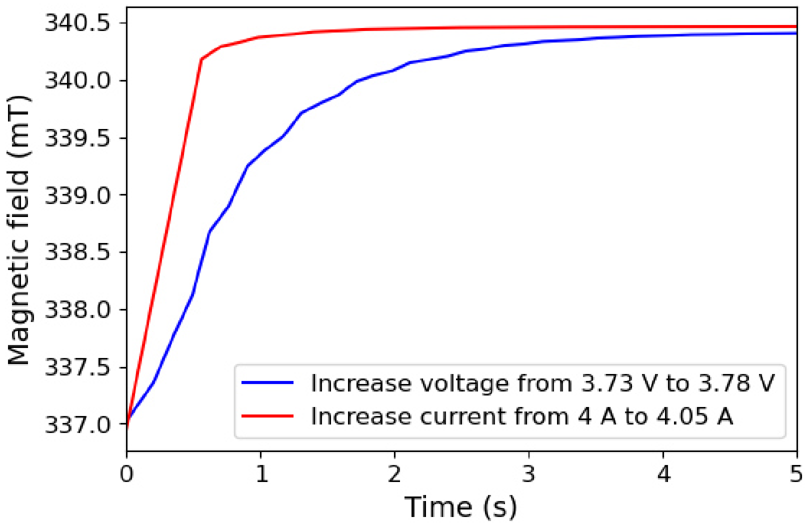

Figure 4.17: Comparison of delay in operational modes of Kepco BOP20-20DL current source.

Due to the limited space between the poles of the magnet, the Hall probe of the teslameter had to be positioned on the side of one of the poles. Measurements with a second Hall probe were conducted to correlate the measured field with the field at the sample location. The relationship between these two fields is displayed in Figure 4.18 and was fit with a linear function. This function is implemented in the "LakeShoreF41()" class of its driver when calling the "read_field_inside()" method. On the other hand, calling the "read_field()" method returns the field located at the Hall probe.

Listing 4.4 shows the driver used for the magnetic field stabilization. It utilizes the custom driver library "maglab" and first initializes the current source and the teslameter. Then, three functions are used to readjust the field by either increasing or decreasing the current. The code shown here focuses solely on stabilization when the magnetic field

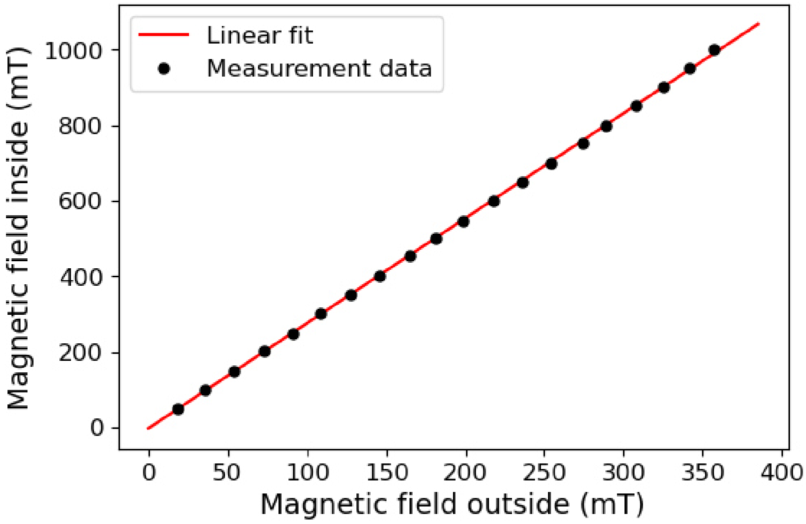

Figure 4.18: Fitting of the magnetic field at the side of the magnet pole (outside) to the field at the sample (inside).

is already close to the desired value. The magnetic field was maintained at 350 mT by adjusting the current of the Kepco BOP20-20DL current source in 0.1 mA increments. Because of these small increments, the time between adjustments for stabilization is reduced to 0.5 s. The driver is capable of stabilizing the field to a tolerance of ±0.012 mT.

```
import maglab as ml
import maglab.logging as logging
import time

ls = ml.LakeShoreF41()
kepco = ml.KepcoBob20()

def increase_field(current, field, step):
    while ls.read_field_inside() < field:
        current = current + step
        kepco.set_current(current)
        time.sleep(0.5)

    return current

def decrease_field(current, field, step):
    while ls.read_field_inside() > field:
        current = current - step
        kepco.set_current(current)
        time.sleep(0.5)

    return current

def readjust_field(field, step, tolerance):
```

```python
    if abs(field - ls.read_field_inside()) < tolerance:
        time.sleep(0.1)
        return

    current = kepco.read_current()
    if ls.read_field_inside() > field:
        current = decrease_field(current, field, step)
    elif ls.read_field_inside() < field:
        current = increase_field(current, field, step)

    return

while True:
    readjust_field(350, 0.0001, 0.012)
```

Listing 4.4: Magnet driver used for magnetic field stabilization.

5 Results

Before presenting the results for the different functionalities in detail, the first two sections of this chapter introduce the two optimization algorithms, illustrated through the example of a notch filter. Notch filters, which are designed to reject frequencies in a narrow band while passing the remaining spectrum, play a crucial role in various signal processing applications.

Following this, a detailed analysis of the notch filter results across multiple frequencies within the spin-wave spectrum is provided, highlighting their effectiveness over a broad range of spin-wave wavelengths. Additional investigations were conducted on the impact of spin-wave excitation power in creating functionalities, demonstrating the strength of the nonlinearity of spin waves.

Finally, a more advanced functionality is demonstrated by utilizing two output antennas to create a frequency demultiplexer, which routes input frequencies to their designated outputs. This showcases the potential of the inverse-designed magnonic processor to handle complex signal processing tasks.

5.1 Direct Search (DS) Algorithm

Direct algorithms follow deterministic procedures and are frequently used for objective functions where derivatives are not available. These methods are also known as "pattern search" techniques, as they often utilize geometric patterns when exploring the search space [44].

The workflow of the direct search (DS) algorithm is illustrated in Figure 5.1. The optimization process begins with a random current configuration, I_0, where $I_0(n)$ represents the current at the n-th loop. The setup consists of 49 DC current loops, so $n = 1, 2, \ldots, 49$. The initial values are randomly selected from a predefined set $S = \{i_1, i_2, \ldots, i_k\}$, resulting in $|S|^{49}$ degrees of freedom, with $|S|$ being the cardinality of the set.

Once the initial configuration is generated, it is applied to the current sources, and a frequency sweep is performed using the VNA to obtain the transmission S_{21} from the input to the output. This transmission is then compared to the reference spectrum S_{21}^{ref}, measured without the influence of the current loops. The comparison is made using an objective function that determines the optimized functionality. In this case, for a notch filter, the objective function

$$O^{\mathrm{DS}} = \left(S_{21}^{\mathrm{ref}} - S_{21}^{\mathrm{I_{app}}}\right)_{\mathrm{filter\,BW}} \tag{5.1}$$

was used to maximize the attenuation of the spin wave signal within the filter's bandwidth. The initial configuration now serves as a baseline, and the actual optimization process begins. The DS optimizer randomly selects a current loop n with its applied current i_j and assigns a new current value randomly chosen from the remaining set $S - \{i_j\}$. The transmission of this new state $\tilde{I}_0$ is measured again, and the objective function is evaluated. If the new objective $\tilde{O}$ is greater than the current objective O, the new best objective value is updated ($O = \tilde{O}$), and the new best configuration found is set as $I_0 = \tilde{I}_0$. If $\tilde{O} < O$, the change is not accepted. Then, the next current loop n is chosen, and the optimization process repeats. Each current loop n is selected once until there has been one attempted change per loop, completing the first iteration of the optimization. The optimized state of iteration 0, I_0, is then set as the starting configuration I_1 for iteration 1. This process is repeated a specified number of times or until a desired objective value is reached.

A 5 MHz bandwidth notch filter example is given in Figure 5.2 at a center frequency of 5.1825 GHz, using input IN_2 and output OUT_3. It shows the reference spectrum S_{21}^{ref}, the best configuration achieved in the 0th iteration with an objective value of 8.34, and the final optimized state after 12 iterations with an objective value of 39.50. The currents were picked from the set $S = \{300\,\mathrm{mA}, 0\,\mathrm{mA}, -300\,\mathrm{mA}\}$ of only three values resulting in $3^{49} \approx 2.39 \times 10^{23}$ degrees of freedom. The current configurations I_0 and I_{12}, which create the spectra, are also displayed on the right side of the figure. A maximum attenuation of 56.39 dB was achieved inside the bandwidth compared to the reference signal. Figure 5.3 illustrates how the objective value evolves over the iterations.

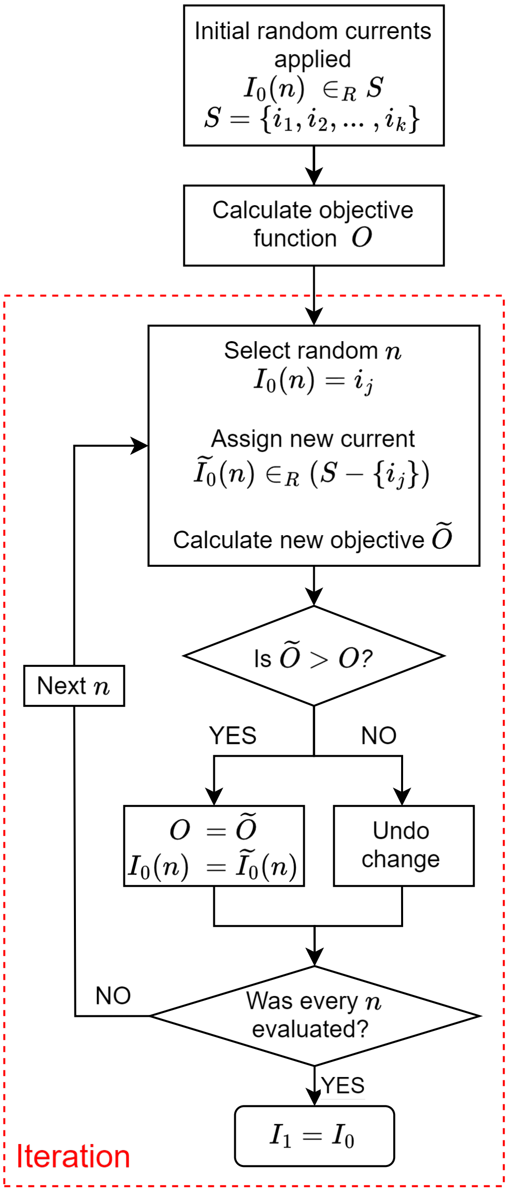

Figure 5.1: Flowchart illustrating the steps of the direct search algorithm. Starting with a random initial configuration, the state is iteratively altered by changing only one variable at a time.

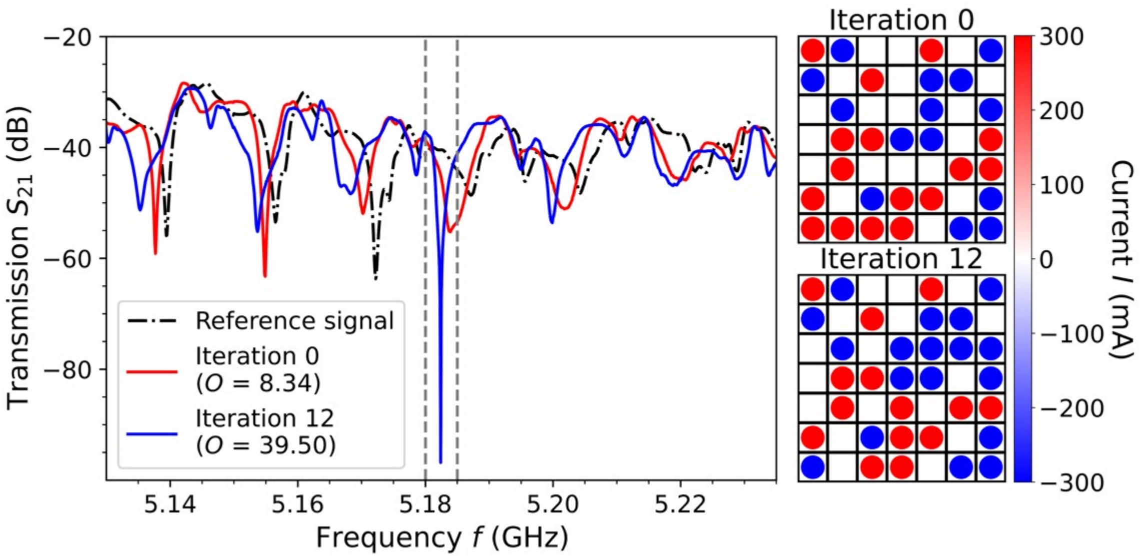

Figure 5.2: Transmission spectra of a reference signal, the best state of iteration 0, and the final state of iteration 12 for a 5 MHz bandwidth notch filter at a center frequency of 5.1825 GHz. The corresponding current configurations for these spectra are shown on the right.

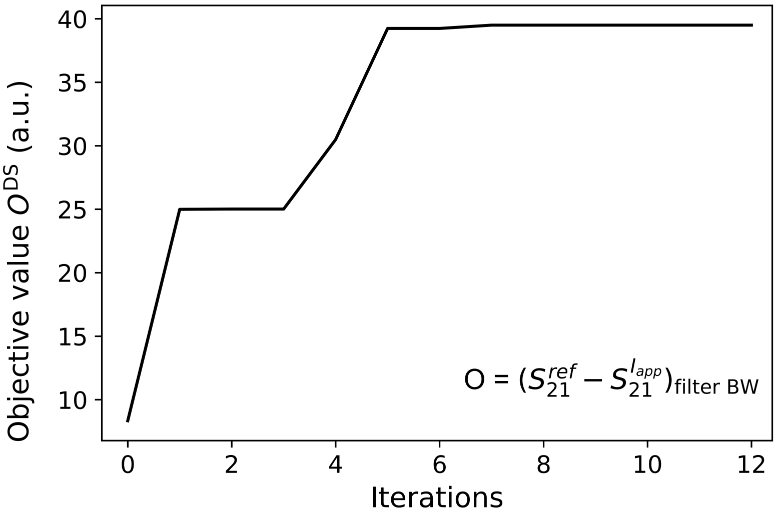

Figure 5.3: Evolution of the objective value O^{DS} with respect to iteration number.

5.2 Genetic Algorithm (GA)

Population-based optimization algorithms, such as genetic algorithms (GA), are stochastic methods that utilize a population of candidate solutions to explore the search space. These algorithms are inspired by nature and fall under the broader category of evolutionary algorithms. Rooted in Darwin's theory of "survival of the fittest", GAs operate on the principle of natural selection. By maintaining a diverse pool of candidates, population-based algorithms enhance robustness and increase the likelihood of finding an optimal or near-optimal solution. They excel in tackling complex problems with noisy evaluations and multiple optima, where traditional methods may be less effective [44, 45].

The GA utilized in this study is implemented using the open-source Python library PyGAD [46, 45]. The workflow is shown in Figure 5.4, which outlines the entire optimization process. The GA begins with an initial population consisting of l random current configurations $I_1, I_2, \ldots, I_l$. Each configuration consists of n variables, referred to as genes in the GA context. Each gene corresponds to a specific current loop and is selected from a predefined set $S = \{i_1, i_2, \ldots, i_k\}$. After evaluating each configuration using the objective function, or fitness function as termed in PyGAD, m parents are chosen to produce the next generation. This new generation is created through crossover and mutation processes applied to the parent configurations, resulting in l offspring configurations. These offspring are then evaluated, and the selection process for parents is repeated. The optimization process continues until either a predefined number of generations is reached or a desired objective value is achieved, resulting in the final optimized current configuration $I(O_{\max})$.

A 5 MHz bandwidth notch filter example is given in Figure 5.5 at a center frequency of 5.0925 GHz, using input IN_2 and output OUT_3. In this case, the objective function

$$O^{\mathrm{GA}} = \left(S_{21}^{\mathrm{ref}} - S_{21}^{\mathrm{I_{app}}}\right)_{\text{filter BW}} - \left|S_{21}^{\mathrm{ref}} - S_{21}^{\mathrm{I_{app}}}\right|_{\text{non filter BW}}, \tag{5.2}$$

not only focuses on maximizing attenuation within the filter bandwidth but also incorporates an additional goal: minimizing signal variation outside the filter bandwidth. It shows the reference spectrum S_{21}^{ref}, the best configuration achieved in the 0th generation with an objective value of 13.33, and the final optimized state after 150 generations with an objective value of 43.08. On the right side of the figure the corresponding current configurations are shown. The optimization utilized the current set $S = \{300\,\mathrm{mA}, 280\,\mathrm{mA}, \ldots, -280\,\mathrm{mA}, -300\,\mathrm{mA}\}$, resulting in $31^{49} \approx 1.19 \times 10^{73}$ possible configurations. A population size of $l = 50$ was used, with $m = 10$ parents selected to generate offspring. The offspring were created through single-point crossover with a mutation rate of 10%. A maximum attenuation of 49.17 dB was achieved inside the bandwidth compared to the reference signal. Figure 5.3 illustrates how the objective value evolves over the iterations.

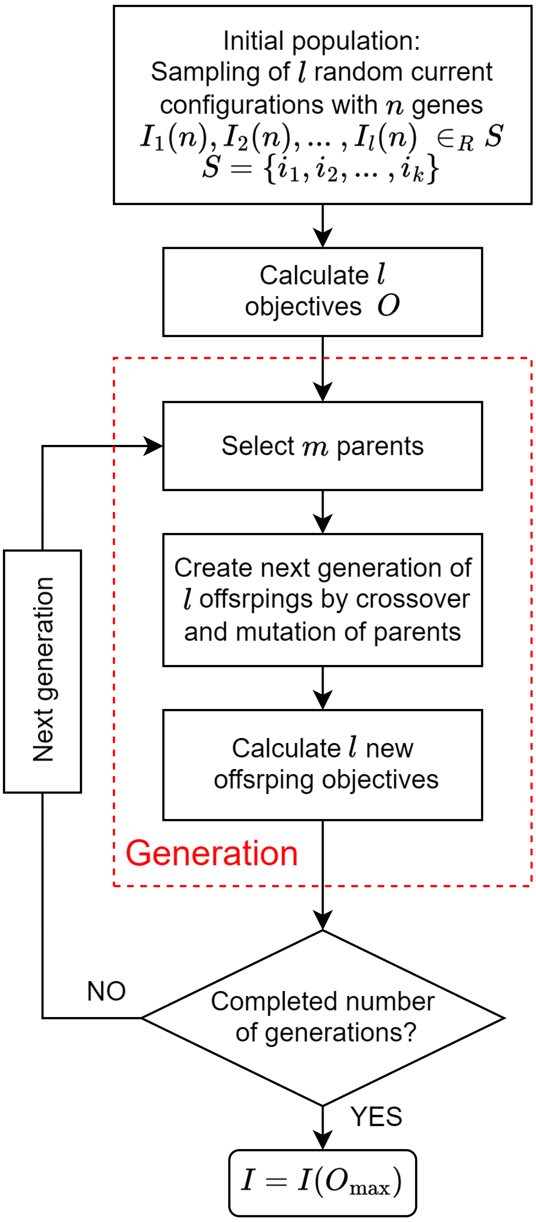

Figure 5.4: Flowchart illustrating the steps of the genetic algorithm. Starting with a random initial population, new states are generated by crossover and mutation of the parent configurations.

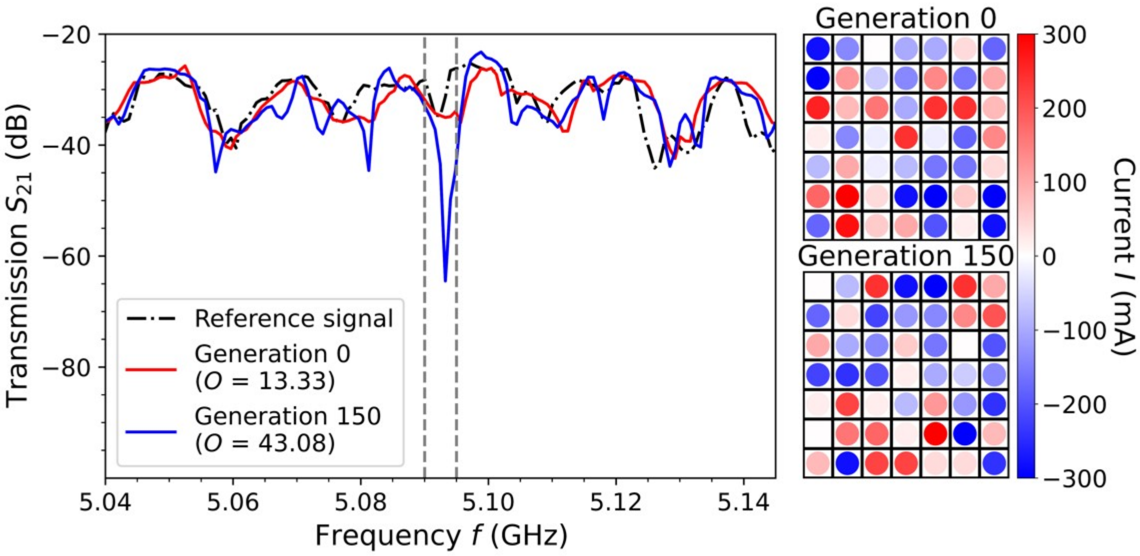

Figure 5.5: Transmission spectra of a reference signal, the best state of generation 0, and the final state of generation 150 for a 5 MHz bandwidth notch filter at a center frequency of 5.0925 GHz. The corresponding current configurations for these spectra are shown on the right.

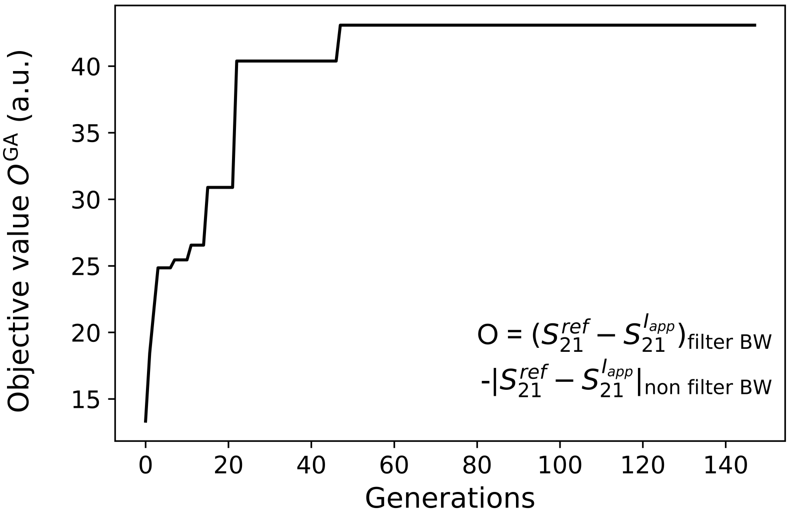

Figure 5.6: Evolution of the objective value O^{GA} over the generations.

5.3 Notch Filter

The notch filter is the first functionality demonstrated with the inverse-design device. A notch filter is designed to reject a narrow frequency band while passing the remaining spectrum. The results are depicted in Figure 5.7 for a microwave power of 0 dBm in the linear regime and in Figure 5.8 for 15 dBm in the weakly-nonlinear regime.

The GA was utilized with the same settings and objective function described in Section 5.2. A notch filter bandwidth of 5 MHz was set and notch filters at various center frequencies spanning from 5.0925 GHz to 5.3325 GHz in 30 MHz steps were realized. These frequencies cover the spin-wave wavelength range of 74.5 µm up to 118.1 µm. Instead of displaying the transmission spectra, like in Figure 5.5 and 5.2, the difference between the reference and the solution state $\Delta S_{21}\,(\mathrm{dB}) = \left(S_{21}^{\mathrm{ref}} - S_{21}^{\mathrm{I_{app}}}\right)$ is used to calculate the attenuation power ratio:

$$\frac{S_{21}^{\mathrm{I_{app}}}}{S_{21}^{\mathrm{ref}}} = \frac{1}{10^{\left(-\frac{\Delta S_{21}\,(\mathrm{dB})}{10}\right)}}. \tag{5.3}$$

An average attenuation of $1.64 \cdot 10^4$ for a power of 0 dBm and an average attenuation of $2.54 \cdot 10^4$ for a power of 15 dBm were achieved.

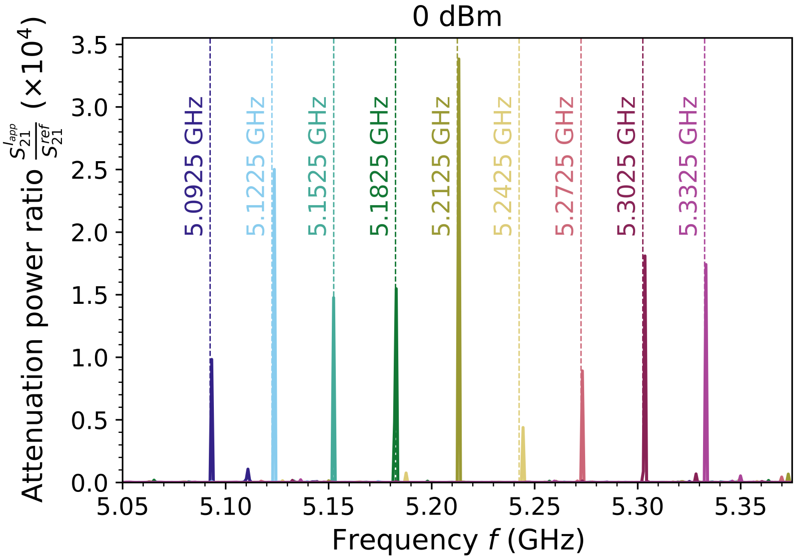

Figure 5.7: Summarized plot of all notch filters at microwave power of 0 dBm showing the attenuation power ratio $S_{21}^{\mathrm{I_{app}}}/S_{21}^{\mathrm{ref}}$. Dashed lines indicate the center frequencies of the notch filters.

The results indicate that the achieved functionality is consistent across a broad spectrum, regardless of wavelength. However, the wavelengths examined are considerably smaller than the characteristic dimension of the field inhomogeneity, $a = 0.531$ mm (see

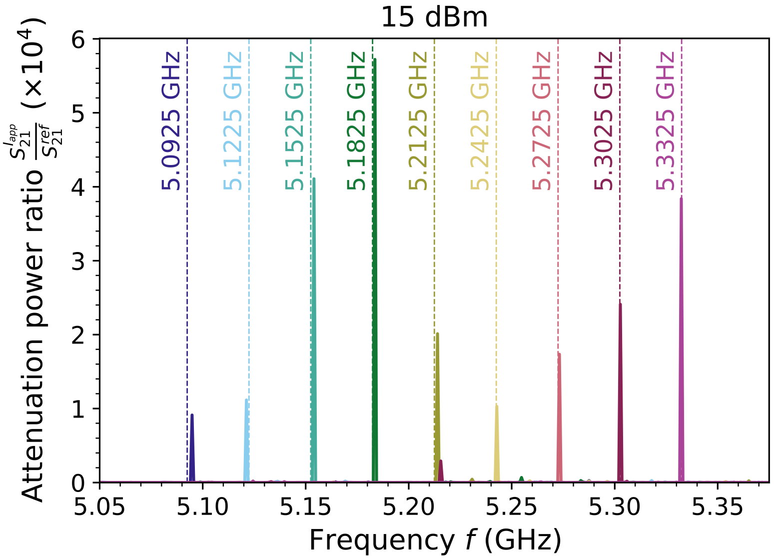

Figure 5.8: Summarized plot of all notch filters at microwave power of 15 dBm showing the attenuation power ratio $S_{21}^{\mathrm{I_{app}}}/S_{21}^{\mathrm{ref}}$. Dashed lines indicate the center frequencies of the notch filters.

Figure 4.14). This lead to further investigations into spin waves with larger wavelengths. Figure 5.9 presents the results for spin-wave wavelengths ranging from 0.365 mm up to 1.260 mm at the power of 15 dBm. Instead of spacing in frequency, steps in wavenumber of approximately 40 rad cm^{-1} were used. The notch filters for large wavelengths were also successfully realized, achieving attenuation greater than $1 \cdot 10^4$ for all wavelengths except $\lambda = 1.260$ mm. At this particular wavelength, the attenuation power ratio significantly decreased to 198.

The results are summarized in Tables 5.1 and 5.2, which present $\Delta S_{21,\mathrm{max}}$ (dB) and $S_{21}^{\mathrm{I_{app}}}/S_{21}^{\mathrm{ref}}$ for power levels of 0 dBm and 15 dBm, respectively. The results indicate that increasing the power, which moves the system into the weakly-nonlinear regime, also enhances its functionality. Further investigations involved the realization of notch filters across a range of microwave powers from −15 dBm to 30 dBm. The results are illustrated in Figure 5.10. For each power level, five notch filters were implemented at a center frequency of 5.1775 GHz, resulting in a total of 50 notch filters. The same initial population was used for all optimizations, and a fixed number of 50 generations was used. Each data point represents the average maximum objective value of the five notch filters at a given power, with error bars indicating the standard deviation of these values. The highest objective values were observed at a power of 25 dBm.

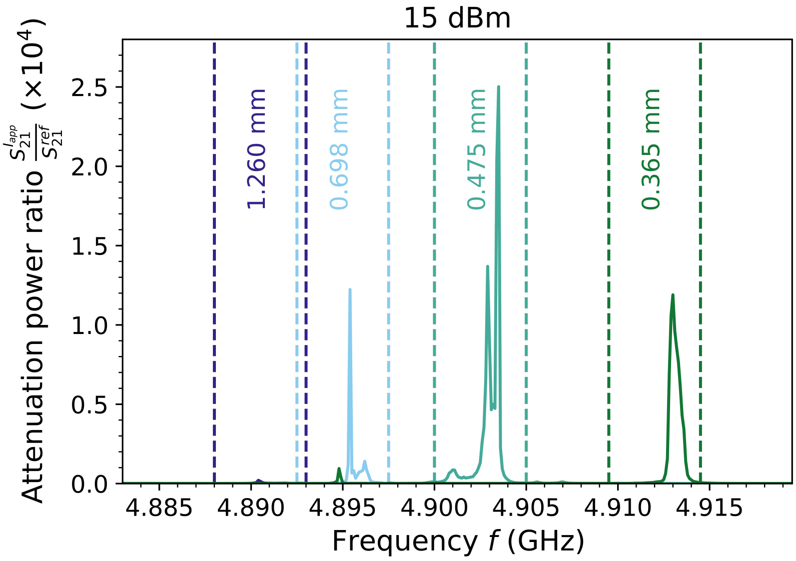

Figure 5.9: Summarized plot of the large spin-wave wavelength notch filters at microwave power of 15 dBm showing the attenuation power ratio $S_{21}^{\mathrm{I_{app}}}/S_{21}^{\mathrm{ref}}$. Dashed lines indicate the defined bandwidths of 5 MHz.

Table 5.1: Summary of notch filter results at 0 dBm power in the linear regime.

f_{center} (GHz)	k (rad cm^{-1})	λ (µm)	$\Delta S_{21,\mathrm{max}}$ (dB)	$S_{21}^{\mathrm{I_{app}}}/S_{21}^{\mathrm{ref}} \times 10^4$
5.0925	531.8	118.1	39.92	0.98
5.1225	574.7	109.3	43.98	2.5
5.1525	615.7	102.0	41.69	1.48
5.1825	655.5	95.8	41.9	1.55
5.2125	694.4	90.5	45.29	3.38
5.2425	732.5	85.8	36.42	0.44
5.2725	770.0	81.6	39.5	0.89
5.3025	807.1	77.8	42.57	1.81
5.3325	843.9	74.5	42.41	1.74

Table 5.2: Summary of notch filter results at 15 dBm power in the weakly-nonlinear regime.

f_{center} (GHz)	k (rad cm^{-1})	λ (µm)	$\Delta S_{21,\text{max}}$ (dB)	$S_{21}^{\text{I}_{\text{app}}}/S_{21}^{\text{ref}} \times 10^4$
4.8905	49.9	1260.4	22.97	0.02
4.895	90.0	697.8	40.87	1.22
4.9025	132.4	474.5	43.98	2.5
4.912	172.0	365.4	40.75	1.19
5.0925	531.8	118.1	39.6	0.91
5.1225	574.7	109.3	40.47	1.12
5.1525	615.7	102.0	46.14	4.11
5.1825	655.5	95.8	47.57	5.72
5.2125	694.4	90.5	43.03	2.01
5.2425	732.5	85.8	40.12	1.03
5.2725	770.0	81.6	42.39	1.73
5.3025	807.1	77.8	43.82	2.41
5.3325	843.9	74.5	45.84	3.84

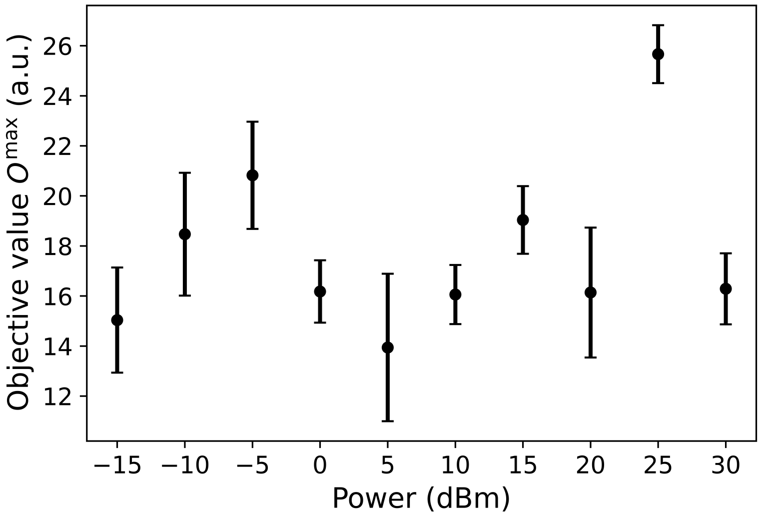

Figure 5.10: Relationship between the microwave power used for spin-wave excitation and the maximum objective reached for a notch filter at center frequency of 5.1775 GHz. Each point displays the average objective reached over five optimizations with the same initial population. The error bars represent the standard deviation of the mean objective value.

5.4 Frequency Demultiplexer

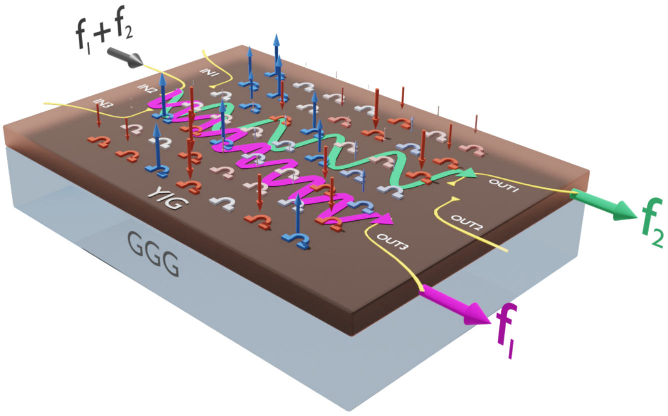

Figure 5.11: Illustration of the working principle of the two-port frequency demultiplexer. Two frequencies f_1 and f_2 are excited at input IN_2 and are guided to their outputs OUT_1 and OUT_3 by the design region, while suppressing the other frequency.

The second functionality demonstrated is a frequency demultiplexer. Figure 5.11 illustrates the operational principle of the two-port frequency demultiplexer. Frequencies f_1 and f_2 are excited at input IN_2 and then detected at outputs OUT_1 and OUT_3. The design region is configured to attenuate f_1 at OUT_1 while maintaining high transmission at OUT_3, and conversely, to attenuate f_2 at OUT_3 while ensuring high transmission at OUT_1.

The demultiplexer was realized by defining two 5 MHz frequency ranges, centered at $f_1 = 5.1525\,\mathrm{GHz}$ and $f_2 = 5.1825\,\mathrm{GHz}$. As with the notch filter, reference signals were used for comparison against the altered signals. The DS algorithm was then employed for optimization, utilizing the objective function

$$O^{\mathrm{DS}} = \left(S_{21}^{\mathrm{ref}} - S_{21}^{\mathrm{I_{app}}}\right)_{f_1,\,\mathrm{OUT}_1} \times \left(S_{21}^{\mathrm{ref}} - S_{21}^{\mathrm{I_{app}}}\right)_{f_2,\,\mathrm{OUT}_3}. \tag{5.4}$$

The objective function was maximized by the algorithm, resulting in attenuation of f_1 at OUT_1 and f_2 at OUT_3. Both components of the objective function were evaluated separately, and configurations where both components resulted in negative values were discarded. The current set $S = \{400\,\mathrm{mA}, 300\,\mathrm{mA}, \ldots, -300\,\mathrm{mA}, -400\,\mathrm{mA}\}$ was used, providing $9^{49} \approx 5.73 \times 10^{46}$ degrees of freedom. Figure 5.12 shows the frequency sweep of the demultiplexer's solution state. The optimization achieved a maximum attenuation of 57.57 dB inside the bandwidth of f_1 at OUT_1 compared to the signal strength of f_1 at OUT_3, and 42.52 dB inside the bandwidth of f_2 at OUT_3 compared to the signal strength of f_2 at OUT_1. Figure 5.13a displays the current configuration of the demultiplexer's solution state, while 5.13b presents a simulation of the magnetic landscape generated by the current loop arrays.

Figure 5.14 provides an alternative view of the frequency sweep, represented as normalized transmission percentages. The 100% transmission value is relative to each output and is normalized within the defined frequency range. This figure demonstrates that the attenuation bandwidth extends beyond the specified 5 MHz window, showcasing the demultiplexer's robustness.

Additionally, Figure 5.15 and Figure 5.16 illustrate the evolution of the transmission S_{21} over the iterations for OUT_1 and OUT_3, respectively. These figures use a colormap to display transmission intensity, with dashed lines indicating the frequency bandwidths. After approximately 35 iterations, regions of low transmission emerge, with −85 dB for OUT_1 and −80 dB for OUT_3, while the other frequency maintains high transmission.

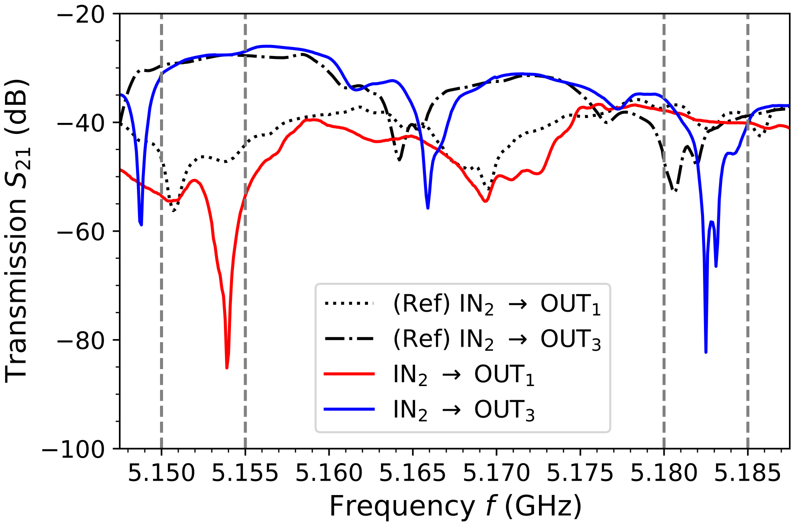

Figure 5.12: Transmission spectra S_{21} of the optimized state and reference signals S_{21}^{ref} for both ports OUT_1 and OUT_3 excited at input IN_2.

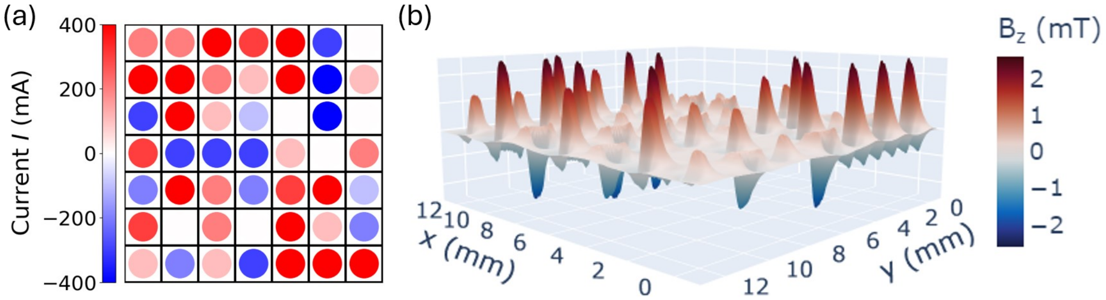

Figure 5.13: The solution configuration optimized by the DS algorithm. (a) The configuration of currents. (b) The magnetic field landscape generated by these currents (simulated with magnum.pi).

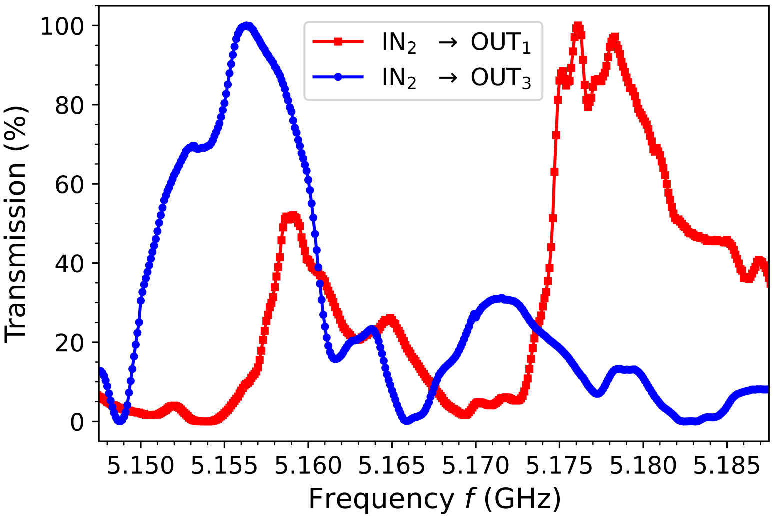

Figure 5.14: Normalized transmission percentage of OUT_1 and OUT_3 as a function of frequency. It highlights the efficient detection of the 5.15 GHz to 5.155 GHz signal at OUT_3, with attenuation at OUT_1. Meanwhile, the 5.18 GHz to 5.185 GHz GHz frequency band is received at OUT_1 and suppressed at OUT_3.

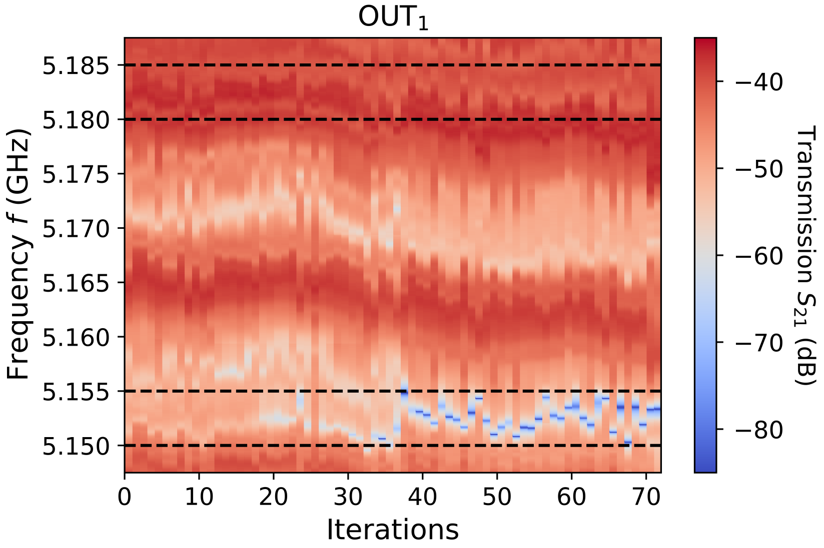

Figure 5.15: Color map depicting the development of frequency rejection bands in the targeted regions as iterations progress for OUT_1.

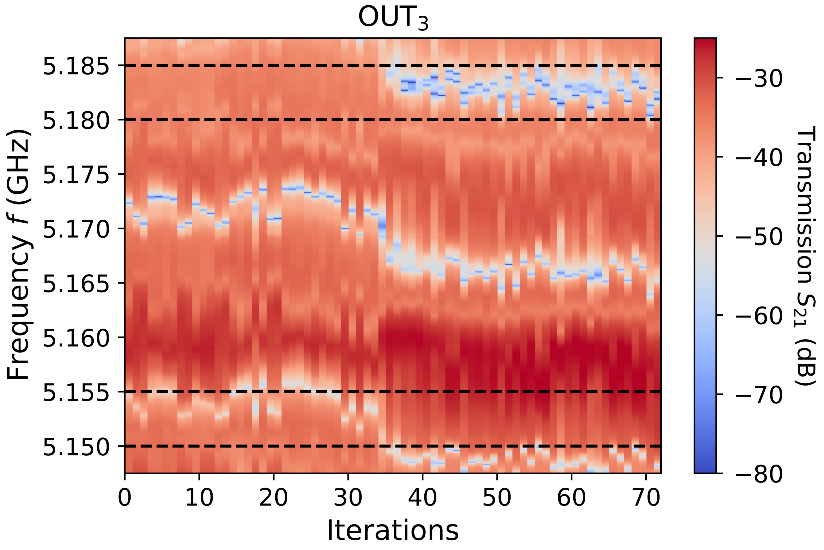

Figure 5.16: Color map depicting the development of frequency rejection bands in the targeted regions as iterations progress for OUT_3.

6 Discussion

6.1 Optimization Algorithms

The two optimization algorithms employed in this study, utilizing fundamentally different approaches, were both successful in creating functionalities. Each algorithm has its own advantages and drawbacks. The DS algorithm, which changes current loops one at a time, has the clear disadvantage of being dependent on the initial random state. For some initial states, no improvements in objective value were found after numerous iterations. To address this, the algorithm was programmed to restart from different initial states if no improvements were made over multiple iterations. Nevertheless, the algorithm is not capable of achieving a global maximization of the objective function, as it tends to stay relatively close to the initial state in the optimization space.

The GA, on the other hand, by mixing a large number of initial states through single-point crossover, is able to explore more of the optimization space. The single-point crossover results in configuration changes of a minimum of one and a maximum of 24 current loops when combining parent configurations. This can be advantageous when exploring the search space but may lack the fine-tuning capability when already near a maximum. This is an advantage of the DS algorithm, as it allows for more fine-tuning by changing variables one at a time, thereby avoiding the risk of taking too large steps in the optimization space.

Other optimization algorithms, such as gradient-based methods that use the first derivative to determine the direction of movement in the search space, were tested but proved unsuccessful. Gradient-based optimizations are typically employed for continuous function optimization, where the derivative can be calculated at any point [44]. Due to the fluctuations encountered in the individual current source channels, the DS and GA utilized steps in current of at least 20 mA. This could be a reason why gradient-based optimizations struggled, as small step evaluations were too noisy to interpret, rendering the search space effectively non-continuous.

6.2 Notch Filter

The notch filters were successfully realized across a broad frequency spectrum, achieving an average attenuation of 41.52 dB at 0 dBm and 43.22 dB at 15 dBm, excluding large wavelengths. These results demonstrate that the realized notch filters perform comparably to industrial notch filters, which typically provide attenuation in the range of −30 dB to −50 dB [47]. An exception occurred at the largest wavelength of 1.260 mm, where attenuation significantly decreased. However, the data representation in Figure 5.9 does not fully account for all relevant details of the data. To address this, Figure 6.1 shows the data as the transmission spectra S_{21}. Despite the frequency band of this notch filter being at the beginning of the spin-wave spectrum, which results in a low-intensity spin-wave signal, the optimization still achieved effective attenuation. The spin-wave signal was reduced to a level comparable to the electromagnetic leakage background, similar to the attenuation level observed in notch filters with wavelengths of 0.475 mm and 0.365 mm. Therefore, the reduced attenuation might be more closely associated with the low intensity of the spin-wave signal rather than with the wavelength.

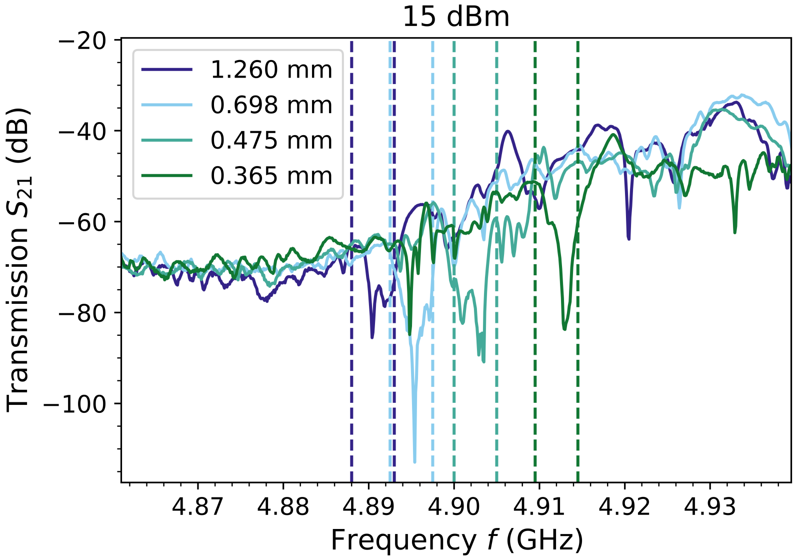

Figure 6.1: Transmission spectra S_{21} of the large spin-wave wavelength notch filters at microwave power of 15 dBm. Dashed lines indicate the defined bandwidths of 5 MHz.

The impact of microwave power on the device's functionality was investigated through a comprehensive study of notch filters (see Figure 5.10). Although the data exhibited some oscillations, indicating that the trend was not entirely clear, a noticeable improvement in functionality was observed in the nonlinear regime at a power of 25 dBm. Since all optimizations began with the same initial population, it is possible that these initial conditions are more favorable for certain microwave powers than for others. To ensure that these improvements were not a result of the initial population, an additional five notch filters were realized at 25 dBm, each starting with a different initial population. The average objective value for these five optimizations was 22.40, demonstrating that 25 dBm consistently enhances functionality. This highlights the significant role of spin-wave nonlinearity in improving device performance. However, increasing the power further to 30 dBm results in a decrease in spin-wave intensity due to increased four-magnon scattering, as discussed in Section 2.4.2. Figure 6.2 illustrates this effect, showing reference spectra at various microwave powers near the center frequency of 5.1775 GHz, where a noticeable decrease in signal strength is observed.

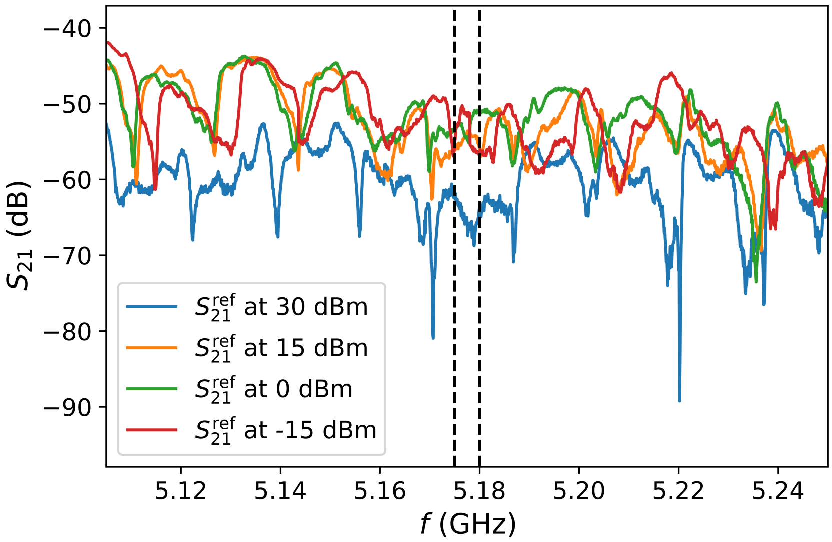

Figure 6.2: Reference transmission spectra S_{21}^{ref} at various microwave powers near the bandwidth of center frequency 5.1775 GHz.

6.3 Optimization Speed

The optimization speed was not prioritized to be as fast as possible since the primary objective of this thesis was to demonstrate a proof-of-concept for the system. For instance, in the DS algorithm example (see Figure 5.2), the optimization explored 588 different configurations over 12 iterations until no further improvements could be made. This process took approximately 35 minutes, with the device requiring 3.6 s to evaluate each configuration.

To maximize insights and learning about the system, the VNA sweeps always covered a 1 GHz window, measuring the full spin-wave spectrum with 10001 frequency points. Reducing the sweep range to the 105 MHz range shown in Figure 5.2 would already result in a 90% reduction in sweep time. Additionally, changes in the experimental setup could further reduce the measurement time significantly. Using single frequency excitation with a signal generator, the fundamental limitation in operational speed would be the inductance associated with the current loops. Studies on dynamic magnonic crystals using high-inductance meanders have shown switching speeds between 5 ns and 10 ns [48, 49]. Achieving similar switching speeds would enable solving the inverse problem in real time.

Regardless of the speed of solving the inverse problem, if solution states for functionalities are already determined for the system, the device can switch between these states on a nanosecond timescale.

The speed of evaluating configurations and the reconfigurability of the device are key advantages of this system compared to the studies discussed in Chapter 3, which rely on both time- and energy-consuming complex numerical algorithms to solve the inverse problem. Additionally, these concepts struggle with limited or non-existent reconfigurability, resulting in fixed functionalities.

6.4 Remeasurability

Figure 6.3 shows some remeasurements of a notch filter at a center frequency of 5.1775 GHz. The reproducibility of the state is evident, but only to some extent. The attenuation within the bandwidth is clearly reproduced, though the level of attenuation varies and some shifting of the signal can be observed. The objective value of these remeasurements varies from 4.92 to 11.62, showing a significant difference from the objective value of 14.61 found in the optimization. These variations in the remeasurements are likely mainly attributed to instabilities in the bias magnetic field and the applied currents. Upgrades to the system, which will be further discussed in the following section, should significantly improve the remeasurability and robustness of the system.

6.5 Future System Upgrades

YIG Sample

The 18 µm thick YIG was selected to maximize the transmission of propagating spin waves. Using an even thicker YIG sample could further increase transmission, as thicker samples result in a steeper dispersion curve, leading to faster spin-wave propagation and higher transmission at the same magnetic damping. Additionally, a larger irradiation volume contributes to increased signal strength.

The low transmission dips in the spectrum, which are due to the hybridization of the fundamental mode with the PSSW modes, do not affect the device's functionality. This has been demonstrated by the effective operation of notch filters over a broad spectrum. For the frequency demultiplexer, even though a low transmission region near the passing frequency of OUT_3 initially had a negative effect, it was optimized to shift to a lower frequency, thus enabling higher transmission at OUT_3 (see Figure 5.16). However, a clearer FVMSW signal would make analysis easier and more clearly show the effects related to the design region.

The coupling to the PSSW modes, which are related to spin pinning at the surface of the film, can be influenced by various treatments. According to the study by J. D. Adam et al. [50], sputtering a 2 µm layer of SiO_2 on a 6.7 µm thick YIG significantly increases the coupling of these modes, resulting in stronger attenuation. Additionally, ion milling 400 Å from the YIG film surface or annealing YIG films at 1000 °C in an oxygen atmosphere for three hours produced similar effects, notably increasing the attenuation notch depth. The study also notes that, without any treatment, variations in the coupling and attenuation notch depth are observed from film to film, with no correlation to substrate preparation or

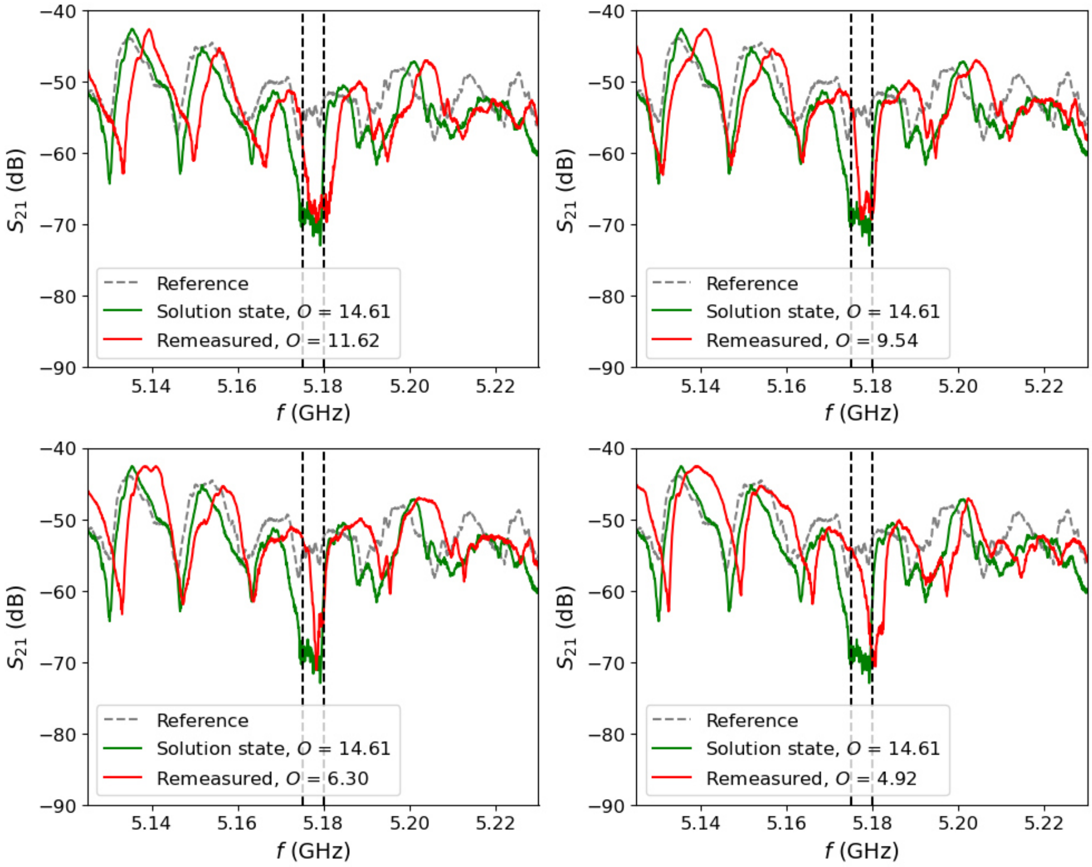

Figure 6.3: Four remeasurement of a notch filter at center frequency 5.1775 GHz. Transmission S_{21} for the reference, the solution state and the remeasurement are shown.

film growth conditions. Therefore, achieving a consistently clear spectrum from samples remains an unresolved issue.

Another study, conducted by Kei Shimada et al. [51], investigated these phenomena through simulated spin-wave transmission. The study identified that transmission ripples were primarily caused by two standing waves originating from the waveguide's edge-edge and waveguide-antenna edge interactions. By incorporating spin-wave absorbers to suppress reflections from the waveguide ends, they achieved a smooth transmission spectrum with the elimination of these ripples.

Spin-Wave Excitation

The transducers used for spin-wave excitation leave room for improvement in their excitation and detection efficiency. Modifying the geometry of the antennas could have significant effects on building functionalities. Lengthening the antennas could increase excitation, resulting in stronger spin-wave signals. Long antennas tend to produce waves that more closely resemble plane waves. However, on the detection side, long antennas could make it harder for the device to create functionalities, as a larger area is used for detection, requiring the device to filter frequencies over a larger spatial region.

Conversely, shortening the antennas could also have interesting effects on the system. Short antennas tend to produce waves that more closely resemble concentric waves. This could be favorable when using wave interference to create functionalities, especially for nonlinear functionalities where multiple inputs are excited simultaneously. Shorter antennas, with their reduced spatial detection region, may also make it easier to filter signals. Additionally, a combination of long antennas for excitation and short antennas for detection is an option worth exploring.

Planned upgrades to the antennas will explore different geometries to investigate their effects. Additionally, the new antennas will feature an aluminum nitride substrate. This substrate is more rigid than duroid, which previously bent easily, making it difficult to ensure proper contact with all antennas simultaneously. The increased rigidity should result in better contact with the YIG sample, leading to reduced insertion losses.

Stability

Even though the magnet stabilization maintains the magnetic field within a tolerance of $\pm 0.012\,\mathrm{mT}$, small shifts in the spin-wave signal of up to $\pm 1.5\,\mathrm{MHz}$ are observed. Compared to the bandwidth of the realized notch filters of $5\,\mathrm{MHz}$, this is a significant shift and can negatively affect optimization and remeasurability capabilities.

To address this, system upgrades are planned to employ a permanent magnet for the bias magnetic field instead of an electromagnet. This change could result in significant improvements in field stability and simplify the setup considerably.

Additionally, the 49 individual current sources, with fluctuations of $\pm 3\,\mathrm{mA}$, present another potential source of instability. However, the effects of current source fluctuations and field stability are interconnected and complex to interpret. After upgrades to the sample and antennas, and the switch to a permanent magnet, these factors will need to be reevaluated and analyzed to determine if further improvements to the current sources are necessary.

7 Conclusion and Outlook

The development of a universal reconfigurable magnonic inverse-design device was successful. Up 10^{73} possible states were utilized in creating functionalities, showcasing the flexibility and capability of the device. Two fundamentally different optimization algorithms were employed and customized for the setup, both demonstrating excellent performance.

Notch filters were realized over a broad range of frequencies, spanning from 4.8905 GHz to 5.3325 GHz, achieving attenuations of up to 48 dB for 5 MHz bandwidths. The device effectively utilized spin waves with wavelengths ranging from 1.26 mm down to 74.5 µm, demonstrating functionality at wavelengths both smaller and larger than the magnetic field inhomogeneity created by one omega loop. This modulation of the signal by more than four orders of magnitude highlights the potential of the concept. The effects of spin wave nonlinearity were studied, showing that an increase in excitation power to 25 dBm resulted in improved functionality, with a decrease observed at around 30 dBm due to increased four-magnon scattering.

Furthermore, a frequency demultiplexer was realized, demonstrating high performance in directing specific spin wave frequencies to designated outputs, while attenuating at least 42 dB at the other output.

Compared to previous work in the field of inverse-design magnonics, this device stands out for solving the inverse problem directly in the experiment, thereby eliminating the need for time- and energy-consuming complex numerical simulations. Additionally, the device enables reconfigurability on a nanosecond timescale, which is challenging to implement in other concepts.

Significant upgrades are planned to enhance the setup's performance. These include the simplification of the bias magnetic field stabilization through the use of a permanent magnet, improvements in signal clarity and strength of the spin wave signal via a different YIG sample, and enhancing excitation and detection through spin-wave transducers with optimized antenna geometry, like variation in antenna length. These advancements are expected to significantly boost the performance of the setup, paving the way for future developments.

In this study, only linear functionalities tailored for RF communication systems, 5G, and future 6G technologies were demonstrated. However, the physics of spin waves offer substantial potential for nonlinear functionalities. The device shows promise for applications in logic gates and reservoir computing, which inherently require nonlinearity to function. Furthermore, it can be utilized in neuromorphic computing applications, such as vowel recognition, where nonlinearity enhances performance. This highlights the device's versatility and potential for broader applications in advanced computational systems.

Bibliography

[1] A. A. Serga, A. V. Chumak, and B. Hillebrands. Yig magnonics. *Journal of Physics D: Applied Physics*, 43, 2010.

[2] Andrii V Chumak. Fundamentals of magnon-based computing.

[3] Gabriel Giribaldi, Luca Colombo, Pietro Simeoni, and Matteo Rinaldi. Compact and wideband nanoacoustic pass-band filters for future 5g and 6g cellular radios. *Nature Communications*, 15(1):304, January 5 2024.

[4] Devaki Chandramouli, Rainer Liebhart, and Juho Pirskanen. *5G for the connected world.* John Wiley Sons, Inc, 2019.

[5] B. Dieny et al. Opportunities and challenges for spintronics in the microelectronics industry. *Nature Electronics*, 3(8), August 2020.

[6] Anjan Barman et al. The 2021 magnonics roadmap. *Journal of Physics: Condensed Matter*, 33(41), August 2021.

[7] A. V. Chumak et al. Advances in magnetics roadmap on spin-wave computing. *IEEE Transactions on Magnetics*, 58(6), 2022.

[8] Alexander Y. Piggott, Jesse Lu, Konstantinos G. Lagoudakis, Jan Petykiewicz, Thomas M. Babinec, and Jelena Vučković. Inverse design and demonstration of a compact and broadband on-chip wavelength demultiplexer. *Nature Photonics*, 9(6), Jun 2015.

[9] Behrad Gholipour, Paul Bastock, Chris Craig, Khouler Khan, Dan Hewak, and Cesare Soci. Microfibers: Amorphous metal-sulphide microfibers enable photonic synapses for brain-like computing (advanced optical materials 5/2015). *Advanced Optical Materials*, 3(5):634–634, 2015.

[10] Alexander N. Tait, Thomas Ferreira de Lima, Mitchell A. Nahmias, Heidi B. Miller, Hsuan-Tung Peng, Bhavin J. Shastri, and Paul R. Prucnal. Silicon photonic modulator neuron. *Phys. Rev. Appl.*, 11:064043, Jun 2019.

[11] Tianwei Wu, Marco Menarini, Zihe Gao, and Liang Feng. Lithography-free reconfigurable integrated photonic processor. *Nature Photonics*, 17:1–7, 4 2023.

[12] Roman Bruck, Kevin Vynck, Philippe Lalanne, Ben Mills, David J. Thomson, Goran Z. Mashanovich, Graham T. Reed, and Otto L. Muskens. All-optical spatial

light modulator for reconfigurable silicon photonic circuits. *Optica*, 3(4):396–402, Apr 2016.

[13] Junwei Cheng, Wenkai Zhang, Wentao Gu, Hailong Zhou, Jianji Dong, and Xinliang Zhang. Photonic emulator for inverse design. *ACS Photonics*, 10(7):2173–2181, Jul 2023.

[14] V V Kruglyak, S O Demokritov, and D Grundler. Magnonics. *Journal of Physics D: Applied Physics*, 43(26):260301, Jul 2010.

[15] Qi Wang, Andrii V. Chumak, and Philipp Pirro. Inverse-design magnonic devices. *Nature Communications*, 12(1):2636, May 2021.

[16] Martina Kiechle, Levente Maucha, Valentin Ahrens, Carsten Dubs, Wolfgang Porod, György Csaba, Markus Becherer, and Adam Papp. Experimental demonstration of a spin-wave lens designed with machine learning, 6 2022.

[17] Ádám Papp, Wolfgang Porod, and Gyorgy Csaba. Nanoscale neural network using non-linear spin-wave interference. *Nature Communications*, 12(1):6422, Nov 2021.

[18] Wolfgang Demtroder. *Experimentalphysik 2, Elektrizität und Optik*. Springer, 2017.

[19] Siegmund Brandt, Hans Dieter Dahmen, Claus Grupen, and Tilo Stroh. Elektrodynamik - von den Maxwell-Gleichungen über die Elektro- und Magnetostatik zur elektromagnetischen Induktion, 2021.

[20] Anil Prabhakar and Daniel D. Stancil. *Spin waves: Theory and applications*. Springer US, 2009.

[21] Claas Abert. Micromagnetics and spintronics: Models and numerical methods. *European Physical Journal B*, 92, 6 2019.

[22] Sergio M Rezende. Fundamentals of magnonics, 2020.

[23] Manuel Hohmann and Martin Von Den Driesch. Mikrowellenspektroskopie, 2005.

[24] Kannan M Krishnan. Fundamentals and applications of magnetic materials.

[25] Philipp Pirro, Vitaliy I. Vasyuchka, Alexander A. Serga, and Burkard Hillebrands. Advances in coherent magnonics. *Nature Reviews Materials*, 6(12):1114–1135, 2021.

[26] Qi Wang, Roman Verba, Björn Heinz, Michael Schneider, Ondřej Wojewoda, Kristýna Davídková, Khrystyna Levchenko, Carsten Dubs, Norbert J. Mauser, Michal Urbánek, Philipp Pirro, and Andrii V. Chumak. Deeply nonlinear excitation of self-normalized short spin waves. *Science Advances*, 9(32):eadg4609, 2023.

[27] H. Schultheiss, K. Vogt, and B. Hillebrands. Direct observation of nonlinear four-magnon scattering in spin-wave microconduits. *Phys. Rev. B*, 86:054414, Aug 2012.

[28] A V Chumak, A A Serga, and B Hillebrands. Magnonic crystals for data processing. *Journal of Physics D: Applied Physics*, 50(24):244001, may 2017.

[29] Lakshmikanta Aditya, Rameshi Meena Meena, Manjeet Ahlawat, P Pareek, P Kulshreshtha, and Rs Shinde. Development of indium doped calcium vanadium garnets for high power cw circulators at 505.8 mhz for indus-2. 1 2018.

[30] Arne Vansteenkiste, Jonathan Leliaert, Mykola Dvornik, Mathias Helsen, Felipe Garcia-Sanchez, and Bartel Van Waeyenberge. The design and verification of MuMax3. *AIP Advances*, 4(10):107133, 10 2014.

[31] Pytorch. `https://pytorch.org/`.

[32] Spintorch. `https://github.com/a-papp/SpinTorch`.

[33] Wavetorch. `https://github.com/fancompute/wavetorch`.

[34] Frank Gustrau. *RF and microwave engineering: Fundamentals of Wireless Communications*. Wiley, 2012.

[35] William H. Hayt and John A. Buck. *Engineering Electromagnetics*. McGraw-Hill Education, 2019.

[36] David M. Pozar. *Microwave engineering*. Wiley, 2012.

[37] Chumakov Dmytro. High frequency behaviour of magnetic thin film elements for microelectronics, 2006.

[38] Dissertation Marc Vogel. Optisch induzierte Magnetisierungslandschaften zur Beeinflussung der Spinwellenpropagation.

[39] B A Kalinikos and A N Slavin. Theory of dipole-exchange spin wave spectrum for ferromagnetic films with mixed exchange boundary conditions. *Journal of Physics C: Solid State Physics*, 19(35):7013, Dec 1986.

[40] A. A. Serga, A. V. Chumak, A. André, G. A. Melkov, A. N. Slavin, S. O. Demokritov, and B. Hillebrands. Parametrically stimulated recovery of a microwave signal stored in standing spin-wave modes of a magnetic film. *Phys. Rev. Lett.*, 99:227202, Nov 2007.

[41] Robert Kraft, Sabri Koraltan, Markus Gattringer, Florian Bruckner, Dieter Suess, and Claas Abert. Parallel-in-time integration of the landau–lifshitz–gilbert equation with the parallel full approximation scheme in space and time. *Journal of Magnetism and Magnetic Materials*, 597:171998, 2024.

[42] Standard commands for programmable instruments (SCPI). `https://en.wikipedia.org/wiki/Standard_Commands_for_Programmable_Instruments`.

[43] PyVISA. `https://pyvisa.readthedocs.io/`.

[44] Ideen Sadrehaghighi. Optimization problem, 2022.

[45] Ahmed Fawzy Gad. Pygad: An intuitive genetic algorithm python library. *Multimedia Tools and Applications*, pages 1–14, 2023.

[46] PyGAD. `https://pygad.readthedocs.io/`.

[47] Joseph J Carr. *The technician's EMI handbook : clues and solutions*. Newnes, Oxford, New Zealand, 2000.

[48] A V Chumak, T Neumann, A A Serga, B Hillebrands, and M P Kostylev. A current-controlled, dynamic magnonic crystal. *Journal of Physics D: Applied Physics*, 42(20):205005, 2009.

[49] Andrii V. Chumak, Vasil S. Tiberkevich, Alexy D. Karenowska, Alexander A. Serga, John F. Gregg, Andrei N. Slavin, and Burkard Hillebrands. All-linear time reversal by a dynamic artificial crystal. *Nature Communications*, 1(1):141, 2010.

[50] J. D. Adam, T. W. O'Keeffe, and R. W. Patterson. Magnetostatic wave to exchange resonance coupling. *Journal of Applied Physics*, 50(B3):2446–2448, 03 1979.

[51] Kei Shimada, Taichi Goto, Naoki Kanazawa, Hiroyuki Takagi, Yuichi Nakamura, Hironaga Uchida, and Mitsuteru Inoue. Extremely flat transmission band of forward volume spin wave using gold and yttrium iron garnet. *Journal of Physics D: Applied Physics*, 50(27):275001, 2017.